

Review

Fabrication of Micro/Nano Structures on Metals by Femtosecond Laser Micromachining

K. M. Tanvir Ahmmed, Colin Grambow and Anne-Marie Kietzig *

Department of Chemical Engineering, McGill University, 3610 University Street, Montreal, QC H3A 0C5, Canada; E-Mails: tanvir.ahmmed@mail.mcgill.ca (K.M.T.A.); colin.grambow@mail.mcgill.ca (C.G.)

* Author to whom correspondence should be addressed; E-Mail: anne.kietzig@mcgill.ca;
Tel.: +1-514-398-3302; Fax: +1-514-398-6678.

External Editor: Cheng Luo

Received: 22 October 2014; in revised form: 13 November 2014 / Accepted: 13 November 2014 /
Published: 20 November 2014

Abstract: Femtosecond laser micromachining has emerged in recent years as a new technique for micro/nano structure fabrication because of its applicability to virtually all kinds of materials in an easy one-step process that is scalable. In the past, much research on femtosecond laser micromachining was carried out to understand the complex ablation mechanism, whereas recent works are mostly concerned with the fabrication of surface structures because of their numerous possible applications. The state-of-the-art knowledge on the fabrication of these structures on metals with direct femtosecond laser micromachining is reviewed in this article. The effect of various parameters, such as fluence, number of pulses, laser beam polarization, wavelength, incident angle, scan velocity, number of scans, and environment, on the formation of different structures is discussed in detail wherever possible. Furthermore, a guideline for surface structures optimization is provided. The authors' experimental work on laser-inscribed regular pattern fabrication is presented to give a complete picture of micromachining processes. Finally, possible applications of laser-machined surface structures in different fields are briefly reviewed.

Keywords: micro/nano structures; femtosecond laser micromachining; surface texturing; metals

1. Introduction

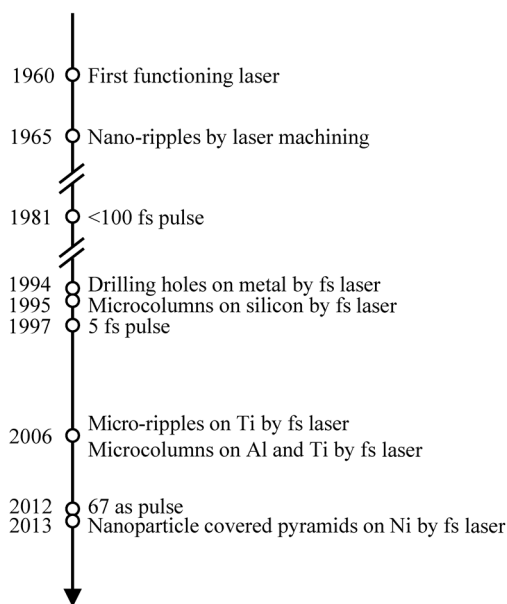
Femtosecond (fs) laser micromachining, a precise machining process of high resolution, has gained considerable attention over the past two decades. Functionalizing a surface by structuring it with a fs

laser dominates the recent research in fs laser micromachining. The properties that can be tailored with surface structuring include electrical, mechanical, chemical, tribological, wetting, and optical. There are various existing and potential applications of laser-textured surfaces based on these modified material properties. Laser textured surfaces exhibiting structural color can act as a permanent paint and might be used for decorative purposes [1,2]. Highly absorptive textured surfaces can find applications in solar cells [3,4] and in stealth technology [5]. Superhydrophobic surfaces fabricated by laser texturing have many applications that include anti-icing, anti-corrosion, self-cleaning, and drag reduction [6–8]. Biomedical applications of textured surfaces include biocompatibility [9,10] as well as reduced or enhanced cell adhesion depending on the types of cells [11–13]. Other applications of textured surfaces include Surface Enhanced Raman Scattering (SERS) effect [14], thermal radiation [15], enhanced photodiode performance [16,17], magnetic data recording media [18], X-ray generation [19], and reduced wear in mechanical parts [20]. These different fields of application require optimized surface structures with different shapes and sizes. Surface structuring can lead to feature sizes smaller than the effective beam diameter, which is referred to as laser-induced structures. However, feature sizes comparable to the effective beam spot size can also be achieved by surface machining, which are referred to as laser-inscribed structures in this review. Fabrication processes of laser-induced and laser-inscribed structures on metals and alloys by direct fs laser micromachining as well as the effect of different laser parameters on structure formation are reviewed in this work.

1.1. Brief History of Surface Structuring with Femtosecond Lasers

The term laser was coined in 1957 [21], which stands for Light Amplification by Stimulated Emission of Radiation. Pulses shorter than 100 fs were first achieved in 1981 using a dye laser [22], two decades after the first invention of the laser in 1960 [23]. Pulses as short as 5 fs were achieved in 1997 with a solid-state Ti:sapphire laser [24], whereas the current record for ultra-short pulse duration has been achieved by Chang’s group with 67 attoseconds (as) [25]. A timeline for the milestones of femtosecond laser micro/nano structuring and other related works is provided in Figure 1.

Figure 1. Timeline of fs laser micro/nano structuring and other related works [5,22–30].



Femtosecond micromachining of metals began in the early nineties; holes were drilled into metals, such as nickel, copper, silver and gold [27,31–33]. Microcolumns on silicon, which were already known to be produced by long pulsed lasers (such as nanosecond lasers), were also fabricated by fs laser machining in 1995 [28]. Modelocked Ti:sapphire systems equipped with chirped pulse amplification (CPA) are the most widely used femtosecond laser systems for material micromachining because of their high intensity, absence of toxic dyes, and wide availability.

1.2. Advantages of fs Laser Micro/Nano Texturing

1.2.1. Comparison with Other Techniques

Micro/nano surface structures can be fabricated by various methods, for example photolithography, X-ray, electron beam, ion beam, particle beam, and mechanical methods. There are some advantages of laser micromachining over other methods to fabricate surface structures:

- The equipment is simpler; there is no need for vacuum or clean room facilities.
- The laser is capable of fabricating the desired micro/nanostructure in a single step process. Hierarchical structures containing both micro- and nanostructures can be created in a single machining step; thus, the process is efficient.
- Machining is performed through a beam of light and thus contactless.
- The process is applicable to the surfaces of any 3D object.
- Many parameters can be easily adjusted resulting in a great variety of possible structures.
- It is possible to lase in many different environments, such as gases, liquids, or in a vacuum and therewith influence the surface chemistry or prevent contamination.

1.2.2. Advantages of fs Pulse over Longer Pulses

Femtosecond lasers offer certain advantages compared to other longer pulsed lasers (e.g., nano- or picosecond lasers). Ablation on virtually any material is possible with fs lasers [34]. The key characteristic of fs lasers is its pulses of high intensity in an exceedingly short time frame, which enables precise ablation of materials and a small heat affected zone (HAZ) [35,36]. For instance, a 1.5 μm wide HAZ was measured on Al after ablation with pulses of 200 fs duration, whereas the measured HAZ was 20 μm for ablation with 8 ns pulses [37]. Thus, nanometer resolution and precision are possible [38,39]. With fs lasers, ablation occurs via fast creation of vapour and plasma with almost no heat conduction, which results in no molten material or recast layer [40]. Because of the aforementioned properties of femtosecond lasers, novel techniques, such as lasing transparent materials can be explored [41,42]. In contrast, lasers with longer pulse durations are incapable of machining as precisely because of photothermal ablation, which results in significant melting in the heat affected area [33].

2. Surface Structuring with fs Laser

Surface structuring with fs lasers is possible in various ways, such as interferometric fs laser structuring [43], direct fs laser writing [44], and fs pulsed laser deposition (fs-PLD) [45]. In this review, we will limit our discussion to surface structuring with direct fs laser writing. Before discussing the

structuring process and machining parameters, it is necessary to revisit laser-matter interactions and to define the threshold fluence for ablation.

2.1. Laser-Matter Interaction and Ablation Threshold

Laser-matter interaction leads to material removal (e.g., ablation) and eventually the formation of micro/nano structures. The mechanism of femtosecond laser ablation depends on material properties, laser properties, and the machining environment. The final modification of the surface depends on the ablation mechanism and experimental parameters. In particular, the threshold value for ablation is a very important parameter for material micromachining. Knowledge of the threshold fluence and the underlying ablation mechanism aids in understanding the role played by various parameters during laser micromachining.

2.1.1. Laser-Matter Interaction

Laser-matter interactions for femtosecond laser irradiation are complex because of the various effects and processes taking place over a short duration of time. The first step of laser-matter interactions is the absorption of photons by electrons. Linear absorption is the main absorption mechanism for metals, whereas for semiconductors, dielectrics, and insulators non-linear absorption is dominant. Photon absorption excites electrons, and on a time scale of 100 fs, thermalization of hot electrons leads to an electron temperature, which is much higher than the lattice temperature. Hot electrons cool down by hot electron diffusion and electron-phonon interaction. Thus, a thermal equilibrium is established between the lattice and the electrons. The so-called two-temperature model is commonly used to explain the temperature dynamics prior to the establishment of a thermal equilibrium between the electrons and the lattice [33,46]. Laser material interaction after a few picoseconds is considered a thermal process, whereas events occurring before are considered non-thermal processes. Time scales for different events of fs laser-matter interaction are discussed by Linde *et al.* (1997) [47].

The interaction between electrons and phonons is very important for microstructuring. For metals with a large electron-phonon (e-ph) coupling constant energy is transferred faster from the electrons to the lattice than for metals with low e-ph coupling constants, and thus no significant amount of heat transfers to the inside of the material for metals with large e-ph coupling constants. As a result, the absorbed energy accumulates near the surface of the material, and leads to laser-induced surface structures due to increased hydrodynamics of the molten material [48]. Thus, transient materials with their large e-ph coupling constant are more prone to forming various surface structures compared to noble materials that have low e-ph coupling constants.

Ablation, the removal of material, occurs on a time scale of 100 ps after a pulse of a fs laser collides with the material [47]. Many ablation mechanisms have been proposed and experimentally verified for femtosecond laser machining; among these the main ablation mechanisms are phase explosion [49], critical phase separation [50], fragmentation [51], spallation [52], melting [53], vaporization [33], and Coulomb explosion [54]. According to the phase explosion model, extreme temperature, pressure, and density are induced in the material under femtosecond laser superheating conditions, and the material is transformed into a superheated liquid. Complicated phase transitions and thermodynamic phenomena, such as the nucleation of bubbles, turn the superheated liquid into a mixture of liquid droplets and vapour,

which expands at high velocity. The ablated material cools down fast and leads to the formation of microstructures on the surface. Hydrodynamics of the molten pool play an important role in structure formation. Redeposition of the ablated particles further dictates the morphology of the irradiated surface.

A more detailed digest of laser-matter interactions is provided by other authors, for example, Shirk *et al.* (1998) discussed the various photon absorption processes [55], whereas Cheng *et al.* (2013) provided a detailed review of ablation mechanisms [56].

2.1.2. Ablation Threshold

The ablation threshold is expressed in terms of peak fluence. The peak fluence of a Gaussian beam is defined as [57,58]:

$$F = \frac{2E}{\pi r_0^2} = \frac{8E}{\pi \omega_0^2} \quad (1)$$

where E is the single pulse energy (J), r_0 and ω_0 are the beam radius and diameter (cm), respectively. For a Gaussian beam, the beam radius is typically expressed by $1/e^2$ definition, *i.e.*, the distance at which the optical intensity of the beam falls to $1/e^2$ or 13.5% of its peak value. The single pulse energy is calculated as:

$$E = \frac{P}{f} \quad (2)$$

where P (Watt) is the average power of the laser beam measured by a power meter and f (Hz) is the frequency (also called repetition rate) of the laser. The fluence, resulting from a certain pulse duration and a fixed number of pulses that is sufficient to ablate a material is termed threshold fluence (F_{th}), or simply ablation threshold. Two different threshold fluences for two different regimes of ablation can be distinguished, as noted by Nolte *et al.* (1997) [35]. The low ablation rate regime (gentle ablation) is characterized by the optical penetration depth, whereas the high ablation rate regime (strong ablation) depends on the effective thermal penetration depth.

The ablation threshold $F_{th}(N)$ for N number of pulses can be related to the single pulse ablation threshold $F_{th}(1)$ according to the following equation, which is based on the accumulation model of Jee *et al.* [59]:

$$F_{th}(N) = F_{th}(1)N^{S-1} \quad (3)$$

where S is the incubation coefficient which characterizes the degree of incubation in the material. This pulse accumulation behavior, also called incubation effect, is widely studied in metals as well as other materials [58,60,61].

An ablation threshold can be determined by various methods that include diameter and/or crater depth (or ablation rate) measurements and laser mass spectrometry. Care must be taken when determining the threshold, as the method of threshold fluence determination might influence the absolute value as pointed out by Mannion *et al.* (2004) [58]. They considered the diameter method of F_{th} determination to be more accurate than the ablation rate method because of higher confidence on diameter measurements compared to the latter. Similarly, in a separate study, Preuss *et al.* (1995) determined the threshold fluence for Ni with mass spectroscopy as 0.02 J/cm^2 , whereas by using a profilometer they detected the ablation at a fluence of 0.34 J/cm^2 [31].

Different micromachining parameters also affect the threshold fluence. Preuss *et al.* (1995) studied the ablation threshold for different metals in vacuum with a laser of 500 fs pulse width and 248 nm wavelength [31]. They observed that for Ni and In the threshold fluence does not change for machining in air compared to in vacuum. In contrast, Gamaly *et al.* (2005) found that the threshold fluence doubled for ablation of Al, Cu, Fe and Pb with a 12 ps laser in air compared to in vacuum [62]. It was further observed that the threshold fluence does not depend on the pulse duration below 100 ps pulses [63]. However, the metal sample thickness plays an important role [64–66]. Threshold fluence increases with increasing sample thickness for metal samples thinner than the hot electron diffusion length (L_c) of the respective metal. Once the sample thickness is larger than L_c , threshold fluence does not vary with thickness anymore, and the fluence is said to be at saturation. Thus, for Au the threshold fluence does not change if the sample is thicker than 800 nm, and for Ni saturation is reached at 50 nm [64]. Yahng *et al.* (2009) studied the effect of the sample temperature on threshold fluence and found that for Si the threshold fluence decreases with increasing temperature from 300 to 900 K, whereas for SS304 no change in ablation threshold was found, but the ablation efficiency increased by 20% [67]. This behaviour can be attributed to the increase in the absorption coefficient at high temperature.

Table 1 tabulates ablation thresholds for several metals and alloys for a single pulse and for hundred pulses.

Table 1. Ablation thresholds for a single pulse and for 100 pulses for different metals ablated with femtosecond lasers. * The authors reported peak fluence values.

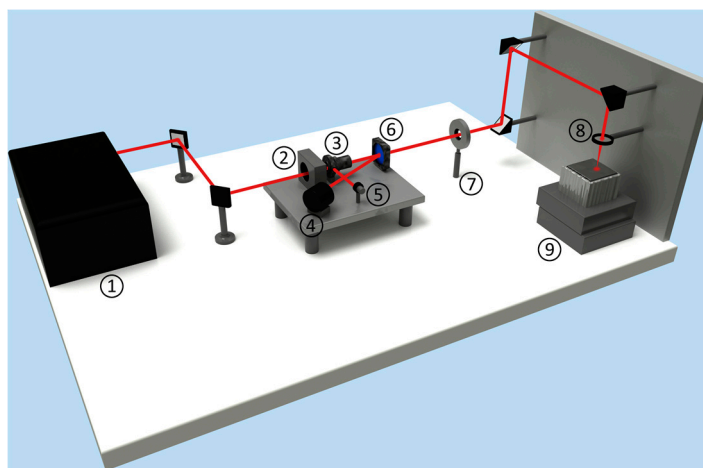
Metals and Alloys	Ablation Threshold, $F_{th}(100)$ (J/cm ²)		Ablation Threshold, $F_{th}(1)$ (J/cm ²)
	In Vacuum [31]	In Air	In Air
Cu	0.170	0.55 * [58]; 0.084 [68]	0.58 * [58]
Au	0.210	0.25 [69]	0.067 [70]
Ni	0.085	-	0.022 [64]
Mo	0.155	-	0.048 [64]
In	0.125	-	-
W	0.4	-	-
Ti	-	0.08 * [58]	0.28 * [58]
SS304	-	-	0.1 [71]
SS316L	-	0.13 * [58]	0.21 * [58]
Nb	-	0.28 * [58]	0.19 * [58]
Al	-	0.55 * [72]; 0.4 [73]	-

2.2. Experimental Procedure and Parameters

A typical setup for surface micro/nano structuring is shown in Figure 2. In such a laser micromachining setup, a lens focuses the laser beam onto the sample. Often, the sample is polished with Silicon Carbide paper followed by a diamond suspension when higher surface smoothness is required. No relative motion between the sample and the beam is needed for drilling holes, but for micromachining a line or patch, relative motion between the beam and the sample is necessary. There are two methods for realizing the relative motion between the beam and the sample: (1) moving the sample under the beam, or (2) moving the beam over the sample. Option (1) requires the translation of the sample by computer-controlled 2D

or 3D stages, whereas for option (2) a two-mirror galvanometric-scanner system moves the beam over the sample. The beam spot size and thus fluence can be controlled in both systems by adjusting the distance between lens and sample. Usually raster scanning is performed to create a patch (area larger than the beam diameter) on the surface.

Figure 2. Typical setup for surface structuring (1) laser, (2) $\frac{1}{2}$ -wave plate, (3) polarizing beam splitter, (4) power meter, (5) beam dump, (6) beam sampler, (7) shutter, (8) focusing lens, and (9) 3-D stage.



The power of the laser beam can be controlled by one of two methods: (1) neutral density filters, or (2) a variable attenuator, which is a combination of a half-wave plate and a polarizing beam splitter, where the polarizer also controls the laser light polarization (shown in Figure 2). A shutter in the beam path can control the number of pulses on a sample. When machining a line or a patch, the number of pulses per spot can also be controlled by varying the scan velocity.

Different diagnostic tools are used with a typical experimental setup. A Frequency Resolved Optical Gating (FROG) monitors the pulse width of a laser beam. Beam shape is analyzed by a beam profiler, which is essentially a charge-coupled device (CCD) sensor that images the attenuated laser beam. A beam sampler/power meter or a beam splitter/power meter combination is used to measure the laser power.

A large number of parameters are involved in laser micromachining. We have classified these parameters in four broad categories: (1) laser beam parameters, (2) sample parameters, (3) scanning parameters, and (4) processing parameters. The average power of the laser beam and thus pulse energy, beam profile, pulse duration, repetition rate, wavelength, polarization of the light, and collimated beam diameter are summarized as laser beam parameters. The sample material and roughness are considered as sample parameters. Scanning parameters include scan velocity, scanner/stage distance from the focusing lens, angle of incidence, overlap, and number of scans (also called overscan). Micromachining environment, gas pressure, temperature of the sample, and mobility of the sample relative to the laser beam (stationary or mobile) are included in the processing parameters. Some of the important parameters along with their definitions are presented in the following paragraphs.

The theoretical beam diameter of a laser beam after passing through the focusing lens is calculated by the following equation [74,75]:

$$\omega_0 = \frac{4\lambda M^2}{\pi d} \quad (4)$$

where l is the focal length of the focusing lens, λ is the wavelength of the laser, d is the input/collimated laser beam diameter onto the focusing lens, and M^2 is the beam propagation factor, which describes the difference between a real laser beam and an ideal diffraction-limited Gaussian beam. Fluence can be changed by changing the distance between the sample and the lens, which alters the beam diameter. The beam diameter at any position y from the focus is given by [76]:

$$\omega_y = \omega_0 \left(1 + \left(\frac{y}{y_R} \right)^2 \right)^{\frac{1}{2}} \quad (5)$$

where y_R is the Rayleigh length given by:

$$y_R = \frac{\pi \omega_0^2}{4\lambda} \quad (6)$$

The fluence (defined in Equation (1)) is the most used laser parameter in micromachining processes. Care should be taken when interpreting this parameter. For a perfect top-hat/flat-top beam, the beam is homogeneous and there is no peak fluence. Thus, the fluence for a flat-top beam is defined as:

$$F = \frac{E}{\pi r_0^2} = \frac{4E}{\pi \omega_0^2} \quad (7)$$

The peak fluence, as already outlined in Equation (1), for a Gaussian beam is twice of the fluence defined in Equation (7). However, some authors use Equation (7) to calculate the “flat-top equivalent” fluence of a Gaussian beam and report it as fluence values [77,78], whereas others use Equation (1) to report peak fluence values [5,58,79–81], while describing the micromachining parameters. The fluence calculated from Equation (7) for a Gaussian beam should be reported as “flat-top equivalent” fluence. However, many authors report fluence values without mentioning any of the descriptive term, *i.e.*, peak or flat-top equivalent. Furthermore, in many cases equations are not provided, thus making it difficult to determine which fluence value is reported. Another laser parameter related to the fluence is the power density, which is the ratio of the peak fluence to the pulse duration. Bizi-Bandoki *et al.* (2013) used this parameter along with the pulse numbers to explain the structure formation by a stationary laser material interaction [82].

Etching a line on a material sample by laser micromachining requires overlapping of pulses (φ_{pulse}) in the scanning direction, whereas fabrication of a patch in a raster scan requires overlapping of pulses in both horizontal and vertical directions on a sample plane. The vertical overlap is termed line overlap (φ_{line}). Pulse overlap and line overlap are respectively calculated as:

$$\varphi_{pulse} = \left(1 - \frac{v}{f \omega_0} \right) \times 100 \quad (8)$$

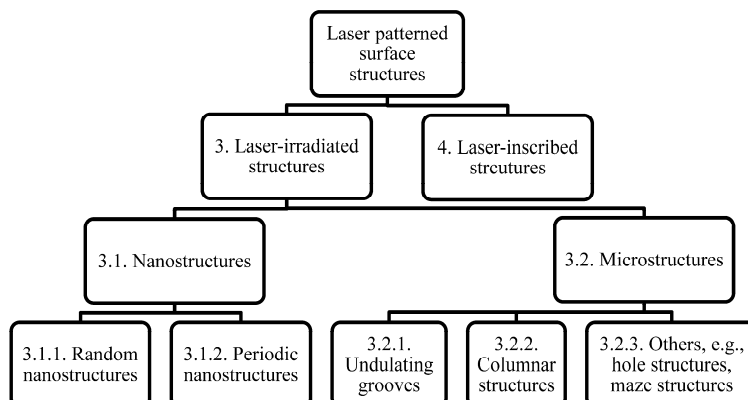
$$\varphi_{line} = \left(1 - \frac{\Delta z}{\omega_{eff}} \right) \times 100 \quad (9)$$

where v is the scan velocity and Δz is the distance between the center of the two overlapping lines. The effective or experimentally obtained line diameter ω_{eff} (also called effective beam diameter) is preferentially used in line overlap calculations instead of the theoretical beam diameter as outlined by Lehr *et al.* (2014) [83]. The difference between the theoretical beam diameter and the effective beam diameter or the line width results from the ablation threshold of the sample material in a given environment and the intensity distribution across the beam when machining with a Gaussian beam. The effective beam diameter is an experimental parameter and varies for different materials and experimental conditions.

3. Laser Irradiated-Surface Structures

Surface micro/nano structuring creates many different structures on various materials. The two broad types are laser-irradiated structures and laser-inscribed structures. The possibilities are limitless for laser-inscribed structures, whereas for laser-irradiated structures only few types of structures are reported. The classification of surface structures is shown in Figure 3.

Figure 3. Classification of laser-patterned surface structures.



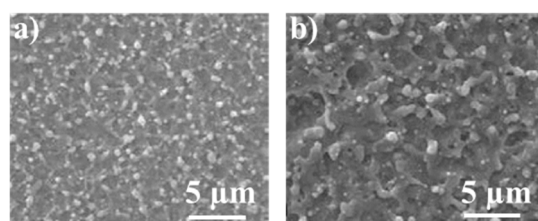
3.1. Nanostructures

Femtosecond direct laser machining can create structures on the nanometer scale. Nanostructures can appear alone or they can be associated with microstructures. The two main types of nanostructures, namely (1) random nanostructures and (2) periodic nanostructures are discussed below.

3.1.1. Random Nanostructures

It is possible to fabricate random nanostructures with a femtosecond laser. The nanostructured surfaces consist of one or more of the following entities: nanoholes, nanocavities, nanoprotusions, nanobumps, and nanorims. Figure 4 shows Scanning Electron Microscope (SEM) images of a Ni surface decorated with nanostructures after micromachining with different fluences. Different mechanisms were proposed to explain the formation of laser-induced nanostructures, such as hydrodynamic processes that originate from localized nanoscale melt, bubble cavitation, and nanoparticle redeposition [68,84–87]. Coloured metals were fabricated by producing nanostructures on the surface. Such structural colors were attributed to the specific nanostructures formed on the metals that induce higher plasmonic absorbance at certain wavelengths [88,89].

Figure 4. Increasing fluence increases feature sizes of nanostructures on Ni, micromachined by a flat-top beam with (a) 1.39 J/cm², and (b) 3.08 J/cm² fluence [87].



The effects of various micromachining parameters on nanostructures formation are discussed in the following sections.

Fluence and Number of Pulses. Nanopores and spherical nanoprotusions on Ti, Au, Cu, and Pt were observed near the ablation threshold and at very low number of pulses [68,84]. Vorobyev *et al.* (2006) noticed that nanostructuring on copper, at the center of the beam spot, is only possible below 1.5 J/cm^2 fluence [68]. The authors observed microstructures beyond this fluence, so there is an upper threshold fluence for nanostructure formation. The size of the nanofeatures increased with increasing number of pulses at a given fluence. A similar trend was observed for a fixed number of laser pulses, where the feature size increased with increasing fluence (Figure 4). Thus, the size and shape of nanostructures can be controlled by varying fluence and the number of pulses. Two effects lead to feature size growth with an increasing number of pulses: (1) enhanced energy absorption, and (2) geometric effect. The enhanced absorption of energy is due to previously generated nanoparticles. The enhancement of laser energy absorption by nanostructures on an Au surface was confirmed experimentally [70]. On the other hand, the geometric effect is caused by the scattered energy due to increased surface roughness. The size of the nanoparticles does not indefinitely increase with number of pulses and fluences. Many of these nanofeatures turned into microstructures with a sufficient number of pulses and value of fluence. The exact magnitude of the latter two parameters depends on the specific material. Surprisingly, the formation of nanostructures was also observed at very high fluence. In one such experiment, at a fluence of 2.9 J/cm^2 with multiple pulses, titanium melted, and a smooth surface with nanostructures of about 10 nm in size was observed [84].

Environment. Fabrication of nanostructures on metals and alloys in different environments was studied in the past. Stratakis *et al.* (2009) obtained nanobumps on Al by fs laser machining (180 fs, 800 nm) in both ethanol and water with a periodicity of 200–300 nm, whereas Al machined in air showed irregular nanoentities of 100 nm in size [89]. The authors have also observed that the periodicity of nanobumps in water and ethanol does not depend on the laser pulse duration, wavelength, or polarization. However, the fluence needed to create nanostructures in air was higher than that required in both ethanol and water. In contrast to the previous study, no ablation was observed for Al in water with a 500 fs 248 nm laser system [88]. However, Dou *et al.* (2003) observed nanostructures on Al2024 alloy in air with a similar laser system having 500 fs pulse duration and 248 nm wavelength [90].

Vorobyev *et al.* (2006) noticed that the gas pressure does not have an effect on the morphology of the nanostructures produced on Platinum [68]. However, the amount of redeposition is higher when machined in air at atmospheric pressure compared to that in vacuum. Plasma expansion can explain this phenomenon. Plasma expands faster and further in vacuum than in air at atmospheric pressure. Thus, the particles have a higher tendency to redeposit when ablated in air.

Others. The influence of pre-structuring on nanostructure formation was studied for Ni machined in ethanol. Nanostructures were formed on the pre-structured material, whereas no nanostructures were observed on the unaltered surface [18]. The morphology of the nanostructures varies with the composition percentage of different metals in an alloy as found by Stratakis *et al.* (2009) on Duralumin alloy ablated in water [88]. Dou *et al.* (2003) also observed the selective ablation of the Al2024 alloy. Accordingly, fs laser microtexturing can be used for surface compositioning, *i.e.*, to change the composition percentage of different metals in an alloy. Li *et al.* (2010) investigated the change of surface chemistry of nanostructures because of the laser ablation of pure Al in air [91]. Crystalline anorthic

Al(OH)₃ and crystalline α -Al₂O₃ were formed by laser irradiation on the Al surface. Typical feature sizes of nanostructures created on different metals and alloys are listed in Table 2 along with the fluence used, and the environment in which they were produced.

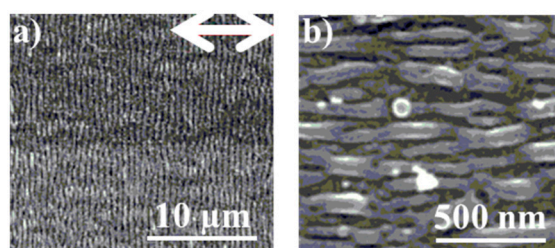
Table 2. Random nanostructures on different metals and alloys with their size, fluence used to produce the features and environment of micromachining. * Values are estimated from the SEM images. n.s. = not specified.

Metals and Alloys	Feature Size (nm)	Fluence (J/cm ²)	Environment	Reference
Ti	≥20	0.067–0.16	Air	[84]
	30–50	n.s.	Vacuum	[92]
Ni	~100–1500 *	1.39–3.08	Air (Flat-top beam)	[87]
	n.s.	n.s.	Ethanol	[92]
Al	~300 *	0.05	Water and ethanol	[88]
	100	0.25	Air	[89]
Al2024	10–500 *	0.2–0.4	Air	[90]
Pt	≥20	0.084–1.52	Air and vacuum	[68]
Cu	≥20	0.084–1.52	Air	[68]
	≤250 (bumps)	0.51	Air	[93]
Ag	≤250 (bumps)	0.51	Air	[93]
Au	≥20	0.084–1.52	Air	[68]
	≤250 (bumps)	0.51	Air	[93]
	≤300 (bumps) *	0.078–1.1	Air	[70]

3.1.2. Periodic Nanostructures

Laser-induced periodic surface structures (LIPSS), also termed ripples or nano-ripples, were first observed in 1965 [26]. LIPSS are periodic nanostructures constituted of alternate crests and troughs. LIPSS produced by long-pulsed lasers have smooth features, whereas LIPSS densely covered with nanostructures are reported for fs pulses [1]. In consideration of periodicity, two distinct types of fs-LIPSS or FLIPSS are observed. The low-spatial-frequency LIPSS (LSFL) have a periodicity close to the laser wavelength. LSFL are perpendicular (\perp) to the polarization of the incident laser beam, *i.e.*, the grating vector of the LIPSS is parallel to the electric field polarization vector of the laser beam. The orientation of the high-spatial-frequency LIPSS (HSFL) that have a periodicity much smaller than the laser wavelength can be parallel (\parallel) or perpendicular to the beam polarization. Figure 5 shows both types of FLIPSS on Ti.

Figure 5. SEM images of (a) low-spatial-frequency LIPSS (LSFL) and (b) high-spatial-frequency LIPSS (HSFL) on Ti irradiated with 790 nm fs laser [80]. The double-sided arrow indicates the polarization of the laser beam.



Spatial energy distribution is assumed to cause FLIPSS formation. According to the classical theory, the interference between the incident laser beam and scattered optical wave at the surface leads to this periodic distribution [94–96]. The periodicity of LIPSS according to the classical interpretation is given by:

$$\begin{aligned}
 &\text{for refraction of } p\text{-polarized beam, } \Lambda_p = \frac{\lambda}{1 \pm \sin\theta} \\
 &\text{for refraction of } p\text{-polarized beam, } \Lambda_p = \frac{\lambda}{n \pm \sin\theta} \\
 &\text{for refraction of } s\text{-polarized beam, } \Lambda_s = \frac{\lambda}{\cos\theta} \\
 &\text{for refraction of } s\text{-polarized beam, } \Lambda_s = \frac{\lambda}{n \cos\theta}
 \end{aligned} \tag{10}$$

where θ is the incident angle and n is the refractive index of the irradiated material. However, this model cannot predict periodicities much smaller than the laser wavelength ($< \lambda/2$), which are only observed for femtosecond laser machining. Other possible mechanisms have been introduced to explain HSFL, such as self-organization [97,98], second-harmonic generation [99], and interference between laser light and surface plasmon polaritons (SPP) [100]. According to the SPP model, the periodicity of the FLIPSS is given by [100,101]:

$$\Lambda = \frac{\lambda}{\text{Re}[\eta] \pm \sin\theta} \tag{11}$$

$$\text{and } \eta = \left[\frac{\epsilon_m \epsilon_d}{(\epsilon_m + \epsilon_d)} \right]^{\frac{1}{2}} \tag{12}$$

Where $\text{Re}[\eta]$ is the real part of the effective refractive index of the metal-dielectric interface for surface plasmons and ϵ_m and ϵ_d are dielectric constants of the metal and of the medium, respectively. Interestingly, Romer *et al.* (2009) observed that LIPSS appear first on grain boundaries for SS316 [102]. The debate of origin and formation of FLIPSS is still ongoing and future investigations are needed to clarify this subject. More details on FLIPSS are presented elsewhere [80].

The effects of various micromachining parameters on LIPSS formation are discussed in the following sections.

Fluence. At a given fluence, LIPSS start to emerge at higher numbers of pulses compared to the numbers of pulses needed for nanostructure formation. The formation of LIPSS at higher fluence starts with a lower pulse number. LIPSS periodicity was studied on Tungsten at different fluences [103]. It was observed that LIPSS periodicity increased with increasing fluence at a constant number of pulses. The dependency of LIPSS formation on fluence was also studied for Mo, Ti and Pt. For all cases, the periodicity increased with increasing fluence [104]. In contrast, the effect of fluence on LIPSS spacing at normal incidence was not detected on SS304 by Groenendijk *et al.* [71]. Thus, the authors suggested that fluence does not directly relate to the LIPSS spacing. However, the effect of fluence was noted on tilted samples. This phenomenon led them to conclude that fluence plays a role in the formation and selection of dominant LIPSS spacing. In addition, the presence of a liquid phase during LIPSS formation was observed in their experiment.

Number of Pulses and Number of Scans. The effect of number of pulses on FLIPSS formation was studied on Pt by a 800 nm fs laser [105]. The periodicity of LIPSS decreased from 620 to 550 nm with the number of shots increased from 30 to 500 at a constant fluence of 0.084 J/cm². Similar results were observed on Tungsten; FLIPSS periods were decreased from 560 to 470 nm [106] and decreased from

600 to 350 nm [103] by increasing the number of pulses from 40 to 800 and 100 to 10000, respectively. An increasing number of scans have a similar effect as a large number of pulses. Decreasing LIPSS periods were observed from 620 to 450 nm with increasing number of scans for a Mg alloy (AZ31B) in air [107].

Angle of Incidence. The effect of angle of incidence on LIPSS periodicity was studied for SS304, Pt, Au, and W with a linearly polarized 800 nm laser beam. The periodicity on SS304 was increased from 670 to 1400 nm and decreased from 670 to 350 nm by tilting the sample from 0° to 50° [71]. Similarly the LIPSS periodicity was increased for gold and platinum from 600 to 3700 nm and 600 to 2800 nm respectively by tilting the sample from 0° to 80° [108]. The periodicity of LIPSS decreased from 528 to 364 nm by increasing the incidence angle from 0° to 70° on Tungsten [103]. The theoretical periodicity did not match the observed periodicity in all four cases stated here. Both models presented earlier (Equations (10)–(12)) cannot accurately predict the observed periodicity. It was suggested that the effective refractive index for the interface is different from the literature value because of the accumulation of nanoparticles on the surface during laser micromachining. Thus, the anomaly in theoretical prediction of LIPSS periodicity.

Wavelength. LIPSS periodicity at normal incidence varies linearly with laser wavelength. LIPSS periodicity dependency on wavelength for tungsten at fundamental and second harmonics laser wavelengths was studied [106]. LIPSS periodicity of 289 and 542 nm were observed for 400 and 800 nm incident wavelength, respectively.

Polarization. The effect of polarization on LIPSS formation at a fluence of 1 J/cm² has been studied for Si. It was observed that the number of pulses needed to form LIPSS with circular polarization (10–30 pulses) is higher than that of linearly polarized laser light (5–15 pulses) [109]. The effect of polarization was also studied on Tungsten using linearly polarized light, elliptically polarized light, as well as left and right circularly polarized light [103]. The LIPSS were angled at +45° and –45° for left and right rotated circularly polarized beams, whereas for an elliptically polarized laser beam the LIPSS were aligned perpendicularly to the long axis. The authors also irradiated a pre-fabricated LIPSS surface and found that the new LIPSS erased the old LIPSS. The orientation of the new LIPSS was defined by the polarization of the final beam.

Scanning Velocity. The effect of scanning velocity on FLIPSS formation was studied on SS301L and Ni at a constant fluence [110]. It was seen that LSFL play a crucial role on the formation of HSFL. With increasing scan velocity, periodic nanostructures appeared on top of the ridges of LSFL and thus formed HSFL with twice the frequency of the LSFL. In a separate study on SS304, it was found that the LIPSS were distorted with decreasing scan velocity at a constant fluence, and undulating grooves started to form perpendicularly to the LIPSS orientation [71].

The above discussion of LIPSS formation was studied in an air environment. However, ablation of Ti submerged in distilled water was studied at low laser power, and LIPSS with a periodicity of 250 nm were observed [44]. Table 3 provides a summary of experimental findings on FLIPSS, their wavelength to periodicity ratio, their orientation, as well as the wavelength and fluence used to generate the features on metals and alloys as determined by different researchers. It is interesting to note that among all metals and alloys most research on LSFL formation was conducted on Ti. Furthermore, with the same 800 nm laser wavelength LSFL with periodicity ranging from 500 to 700 nm were produced [29,84,104,111].

Table 3. Periodic nanostructures reported on different metals and alloys with their wavelength to periodicity ratio, fluence used to produce the features, and orientation relative to the laser polarization at perpendicular incidence. * The authors reported peak fluence values. n.s. = not specified.

Metals	λ/Λ , where $\lambda = 800$ nm (unless specified)	Orientation	Fluence, (J/cm ²)	Reference
Low-Spatial-Frequency LIPSS (LSFL)				
Ti	1.14	⊥	0.25	[29]
	1.51	⊥	0.067–0.084	[84]
	1.6–1.14	⊥	0.09–0.45	[104]
	1.55–1.18 (790)	⊥	0.13 *	[80]
	1.47 (1030)	⊥	0.5	[111]
TA6V	1.33	⊥	2.04	[78]
Ni	1.33	⊥	0.12	[30]
Ni alloy C263	0.99 (775)	⊥	0.28	[60]
Al	1.48	⊥	0.05	[112]
Pt	1.33–1.14	⊥	0.18–0.44	[104]
	1.45–1.29	⊥	0.16	[105]
Cu	2.00–1.18	⊥	0.15–2	[113]
Au	1.38	⊥	0.16	[105]
SS301L	1.23	⊥	0.16	[110]
SS304	1.33–1.19	⊥	0.4–1.1	[71]
AISI 316L	1.60	⊥	0.08–0.2	[114]
	1.45	⊥	2.04	[78]
	1.21	⊥	0.2–2.0	[30]
Mo	1.29–1.14	⊥	0.2–1.1	[104]
W	1.29–1.14	⊥	0.2–1.1	[104]
	2.00–1.33	⊥	2.5–7	[103]
High-Spatial-Frequency LIPSS (HSFL)				
Ti	11.29–8.77 (790)		0.09 *	[80]
Cu	2.96	⊥	0.04–0.1	[113]
SS301L	2.67	⊥	0.16	[110]
W	2.29	n.s.	n.s. (in water)	[92]
Ta	2.29	n.s.	n.s. (in water)	[18]

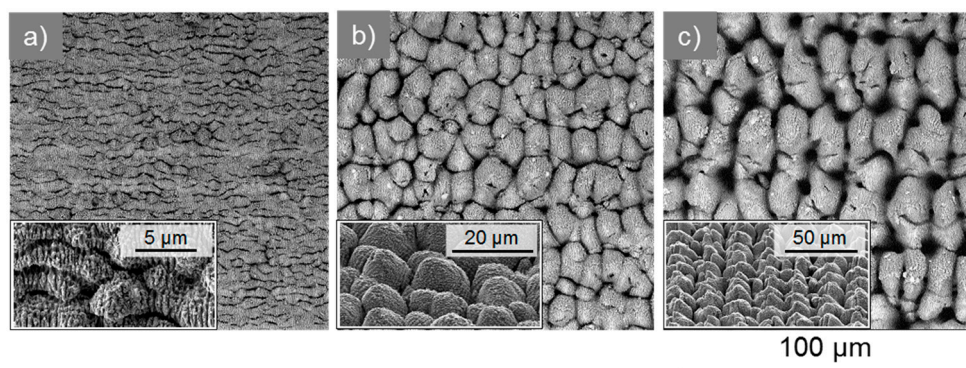
3.2. Microstructures Decorated with Nanofeatures

Fabrication of microstructures on silicon and other materials with fs lasers have been reported since the late 1990s, whereas the metal microstructures, such as undulating grooves and microcolumns, were only reported in the early 2000s. The most commonly reported microstructures originating from laser irradiation on metal surfaces are undulating grooves and columnar structures. These microstructures are often decorated with nanofeatures, such as nano-ripples or nanoparticles.

3.2.1. Undulating Grooves/Micro-Ripples

Periodic grooves perpendicular to the LIPSS were observed on various metals. These undulating grooves, also known as micro-ripples, become deeper and wider with increasing fluence or an increasing number of pulses, which can be achieved by decreasing the scanning velocity or by increasing the overlap in a patch. The undulating grooves are oriented perpendicularly to the LIPSS orientation, *i.e.*, parallel to the laser beam polarization. LIPSS might be superimposed on these undulating grooves. Figure 6a shows the undulating grooves on Ti. The lower threshold fluence for undulating grooves generation is higher than that of higher threshold fluence of LIPSS formation. The formation of periodic grooves was attributed to the spatial energy distribution by the interaction of the laser beam with the surface wave that might be induced by LIPSS [29]. Another possible mechanism for the formation of undulating grooves was attributed to the hydrodynamic processes related to wave phenomena, e.g., capillary waves [78]. An exact theory for explaining the periodicity of undulating grooves is still outstanding.

Figure 6. Laser-induced microstructures on titanium. (a) Undulating grooves covered with LIPSS. Inset: high magnification image. (b) and (c) Columnar structures at single scan and overscan, respectively. Inset: high magnification image of samples tilted at an angle of 40° [48].



The effects of various micromachining parameters on undulating grooves formation are discussed in the following sections.

Fluence. The effect of increasing fluence was reported on SS316L [114]. The width of undulating grooves increased with increasing fluence, thus the periodicity. Eventually, the ridges of the continuous grooves break apart, and become pre-cursor sites for columnar structures.

Number of Pulses. Bizi-Bandoki *et al.* (2011) studied the effect of the number of pulses on undulating grooves on TA6V and SS316 [78]. The periodicity of these grooves increases with the number of pulses. Increasing the number of overscans has a similar effect as increasing the number of pulses, as observed on a Mg alloy AZ31B [107].

Polarization. The effect of polarization on undulating grooves was explored on Ti in vacuum [29]. When the laser beam polarization was rotated, the undulating grooves were also rotated, *i.e.*, the orientation of the undulating grooves was always perpendicular to the laser beam polarization.

Scanning Velocity. Groenendijk *et al.* (2006) reported the effect of scanning velocity on undulating groove formation on SS304 [71]. The authors observed that at constant fluence with decreasing scanning velocity the groove increases in size and eventually the undulating groove structure disappears, forming trenches and columnar structures at low scanning velocities.

It is noticeable from the above discussion that far less work is carried out on undulating grooves formation compared to other laser-irradiated surface structures.

Table 4 summarizes the periodicity for undulating grooves on different metals and alloys together with the fluence values required to generate such undulating grooves on the surface.

Table 4. Characteristics of undulating grooves and columnar structures on different metals and alloys. * Values are estimated from the SEM images.

Metals and Alloys	Periodicity (μm)	Fluence (J/cm^2)	Reference
Ti	1.5–2.4	0.75	[29]
	1.5–4.5 *	1	[111]
Ti-6-4	2.7–3.5	2.04	[78]
AISI 304	1.5–3 *	0.4–1.1	[71]
AISI 304L	2–4 *	0.78–2.83	[115]
AISI 316L	3.5	0.24–0.4 (in vacuum)	[114]
	1.7–2.5	2.04	[78]
Ni	2.5–5	1.392	[87]
AZ31B Mg	1–3	9.5	[107]
FeCuNbSiB	2.7	3.18	[116]

3.2.2. Columnar Structure

The most common microstructures fabricated by femtosecond laser machining are columnar structures as shown in Figure 6b,c. Different names are used to describe these structures, namely, bumpy, cone, spike, mound, and pillar. There is a critical fluence for forming columnar structures. Nayak *et al.* (2010) showed that below this threshold fluence, increasing the number of pulses does not form the regular columnar structures [117]. Usually, nanofeatures decorate the columnar structures. The columnar structure has a distinct stratified shape when laser irradiation interacts with a stationary sample [29,84]. This is attributed to the increased absorption of the laser pulses due to the increased roughness from the previously ablated area by earlier pulses [10]. Geometric effects also play a role due to the variation of the incident angle of the laser beam at the previously ablated location. On the other hand, dynamic interaction, *i.e.*, scanning sample and beam relative to one another, results in columnar structures decorated with LIPSS or nanowhiskers depending on the scanning velocity. This difference between the static and the dynamic interaction is explained later.

Formation of Columnar Structure. Two distinct types of columnar structures are observed on metals and alloys: columnar structures above the initial surface and columnar structures below the initial surface. The formation of microcolumn structures on Ni from different pre-cursor structures, namely, undulating grooves, pits, and random nanostructures were observed by Zuhlke *et al.* (2013) in a series of stop-motion experimentation [87]. At lower fluence, the transition occurred from the undulating grooves, and resulted in below surface growth (BSG) columns. Microdots (small spheres) formed on top of the ridges of undulating grooves. The undulating grooves broke up, allowed larger dots and pits to form. These dots grew in size due to the geometric effect and formed columnar structures. Thus, the valleys were ablated more than the peaks, which explain the increase in height of the columns. However, the laser-irradiated area always depresses the surface with increasing number of pulses. Upon further

increase of the number of laser pulses, the columns started to merge. Ablation is the dominant mechanism in BSG structures, while hydrodynamic processes and redeposition play a minor role.

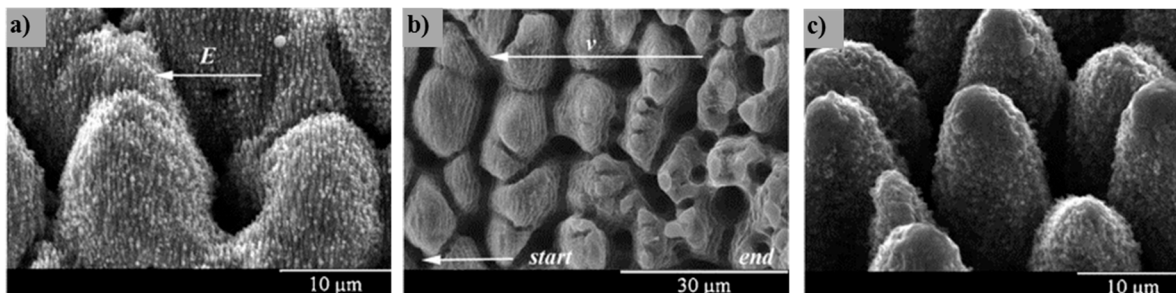
The formation of BSG columns were also observed on Ti [29]. At relatively high fluence, above surface growth (ASG) columns were formed. The actual mechanisms for ASG column formation might vary for different metals and alloys. It is observed that undulating grooves, pits, and dots grew simultaneously for this process on Nickel [87]; however, only pits grew on the surface for SS316 [118]. For the case of Ni, the dots grew in size by the combination of hydrodynamic and particle redeposition processes (termed as vapor-liquid-solid or VLS growth) and turned into columnar structures. The pits grew in size with increasing pulses and eventually devoured the ASG columns. In contrast, the rims of pits joined and formed ASG columns for SS316. Hydrodynamics and VLS growth are also the main growth mechanisms for SS316. Further studies are needed to foster a better understanding on why the process of formation of ASG columns is different for different metals and alloys.

Interestingly, Lehr *et al.* (2014) distinguished between columnar structures from their appearances [83,119]. Pillow-like structures are attributed to those types of columnar structures, where the top of the columns are roundish and the shape of the structures are regular, whereas bumpy structures are more irregular in size. They also observed that pillow-like structures form at lower fluence in comparison to bumpy structures. However, whether the structures are above the initial surface or below the initial surface is not mentioned.

Formation of LIPSS and Nanowhiskers on Top of Columnar Structures. The relative motion between the sample and the laser beam has an effect on the formation of LIPSS and undulating grooves. The effect of scan velocity on different structures has been discussed in previous sections. In this section, the difference between the stationary interaction and the dynamic interaction will be highlighted. In a stationary laser-material interaction experiment, at a sufficient high fluence or high pulse number, the center of the irradiated area does not produce FLIPSS or undulating grooves, instead the undulating grooves and associated LIPSS are observed at the periphery [111]. This phenomenon is due to the energy distribution of a Gaussian beam. At the center of the Gaussian beam, the fluence is higher than the upper threshold fluence for the undulating groove and thus the nano-ripple formation, but at the periphery, the fluence is low enough to match the threshold fluence for undulating groove and LIPSS formation.

For stationary laser material interaction no ripple structures on top of columnar structures are seen, whereas for a dynamic interaction LIPSS decorate the columnar structure (Figure 7a). The fluence to form the columnar structure is higher than that of the upper threshold of the LIPSS formation. During dynamic interaction at low velocity, as the center of the Gaussian beam moves away after forming the columnar structure, the tail of the Gaussian beam creates LIPSS, because its fluence is low enough to match the threshold for LIPSS formation [12,111,114]. Accordingly, at the end of a scan, no LIPSS form, as shown in Figure 7b. This has further been confirmed by experimentation with a Top-hat beam, where the variation of fluence throughout the spot size is almost negligible. Thus, LIPSS on columnar structures were not observed with a Top-hat beam at higher fluence [87]. LIPSS do not always form in a dynamic interaction. Oliveira *et al.* (2009) demonstrated that though the threshold for LIPSS formation was reached, the number of pulses incident on the columnar structure might not be sufficient to produce LIPSS when the scan velocity is very high [111]. In this case, nanowhiskers decorate the columnar structure (Figure 7c). This observation is noteworthy since it highlights that fluence is the necessary but not the sufficient condition for LIPSS formation.

Figure 7. The effect of relative motion on LIPSS formation on Ti samples irradiated at 1 J/cm^2 fluence and with velocity of (a) and (b) $10 \text{ }\mu\text{m/s}$, and (c) $50 \text{ }\mu\text{m/s}$ [111].



The effects of various micromachining parameters on columnar structures formation are discussed in the following sections.

Fluence. There is a lower and upper threshold fluence for columnar structure formation. Columnar microstructures were fabricated on Ti in air above 0.5 J/cm^2 fluence and on Al surfaces below 0.16 J/cm^2 , whereas no microstructures were produced on copper samples [117]. The density of surface features decreased with increasing fluence for Ti. The height of the conical structure, and the spacing between two cones increased with increasing fluence. A similar observation was made on SS316L [114]. Kurselis *et al.* (2012) studied the effect of fluence on the modulation period of microcolumn structures on carbon steel [79]. The authors found that with increasing fluence the amplitude increased up to a certain fluence value, after which the period did not change further. The effect of fluence was also studied for columnar structures on Ti lased in water [44]. The size of the columnar structures increased with increasing laser fluence up to a certain fluence, after which the size of the columns did not change further.

Number of Pulses and Number of Scans. The effect of number of pulses on microcolumns formation was investigated on Ti in a vacuum environment [29]. The periodicity and the distance between micro pillars were increased with a higher number of laser pulses. The effect of overscanning on SS316 was investigated and it was found that the aspect ratio of columnar structures increased with an increasing number of overscans [120]. The effects of overscanning were also studied on Ti and SS304 [48]. It was observed that the microstructure size increased with an increasing number of scans (Figure 6b,c). Similarly, Semaltiano *et al.* (2009) micromachined nickel-based super alloy C263, and found that with an increasing number of overscans the periodicity of the microcolumns increased [60]. Robinson and Jackson (2006) studied the effects of overscanning [121] on Al. The authors found that the unevenness of the textured surface increased with an increasing number of overscans. At higher scanning velocity, the microstructures formed were non-uniform throughout the ablated surface. Higher scanning velocities lowered the severity of surface texturing, but did not completely eliminate the microstructures.

Polarization. The effect of polarization on columnar structures on Ni was investigated with four polarizations: linear polarization P, circular polarization, as well as $+45^\circ$ and -45° rotated from P polarization [122]. The effect of angle of incidence was also studied. At a normal incidence angle, the orientation of the oval base of the conical structures was depended on the beam polarization for linearly polarized light. Similarly, the base of the conical structures was circular for circularly polarized light. The authors found that the shape of the conical structures depended on both the polarization and the angle of incidence. The microstructures were decorated with LIPSS. In contrast, the formation of bumpy

structures was reported on Ti with a circularly polarized light, and instead of LIPSS, 200 nm wide irregular undulations on columnar structures were observed [12]. Kurselis *et al.* (2012) micromachined carbon steel and found that the threshold fluence and overlap to generate microcolumn structures were lower when the polarization was parallel to the scan direction compared to the case where polarization is perpendicular to the motion [79]. The authors suggested that the absorption of energy was higher in the case of motion parallel to the polarization. The threshold fluence was highest for circularly polarized light for fabricating columnar structures. It occurred due to the suppression of the microgroove structure formation near the threshold fluence for a circularly polarized laser beam.

Environment. The effect of different environments, both liquid and gaseous, on columnar structure formation has been studied in the past. Robinson and Jackson (2006) investigated the effect of the gas environment on micromachining of aluminum by using four different gases, namely helium, argon, air, and nitrogen at ambient pressure [121]. It was observed that the recast layer deposits were lowest for the helium environment. The authors did not provide any explanation for their observation.

Nayak *et al.* (2008) studied the formation of conical microstructures in different gas environments on Ti [123]. It was found that micromachining in reactive gases, such as SF₆ and HCl, prevented the formation of conical structures, unlike on Si where columnar structures were observed under such conditions. The density of the pillars was higher in vacuum than in air or helium environments. The conical structures reduced in height but increased in density with increasing gas pressure. It was suggested that the role of the gas environment on structure formation was physical rather than chemical. The formation of conical structures on stainless steel in He, air, SF₆ (at 100 mbar) and in a vacuum (one mTorr) was also investigated [117]. Unlike on Ti, conical structures grew in SF₆ on stainless steel, and the height of the pillars was larger in SF₆ compared to other gas environments. The height and spacing of the conical microstructures increased with the increasing number of laser pulses.

Recently, Lehr *et al.* (2014) extensively studied the effect of different gas environments on columnar structure formation [119]. It was found that Ti ablated in helium and oxygen is covered with TiO₂, whereas Ti machined in nitrogen exhibits TiN in addition to TiO₂. As the modified surface chemistry altered the absorption of laser energy, surface morphologies also varied with the different gas environments. Thus, different machining parameters are needed to fabricate bumpy columnar structures in different gas environments.

Yang *et al.* (2009) also investigated the surface structuring of titanium submerged in different liquid environments at relatively high fluences (3.3 and 9.9 J/cm²) [10]. The authors used distilled water, Hydroxyapatite (HA) solution, and an admixture of CaCl₂ and Na₃PO₄ solution as liquid environments. At low scanning velocity, numerous islands were formed in distilled water. These smooth islands were destroyed at higher velocity and the bumpy structures were decorated with stratified layers. At lower fluence, the structures were smaller than those resulting from machining at higher fluence. Changing the liquid environment from distilled water to HA and admixture of CaCl₂ and Na₃PO₄ solution did not change the morphology of the structures, but it altered the size and density of the features. However, changing the concentration of HA from 0.02 to 0.04 mg/L did not have any noticeable effect on the structures. The formation of structures in liquid was attributed to radiation related ablation along with secondary ablation by the locally generated plasma.

Beam Diameter and Backpressure. The effect of beam diameter was investigated by Kurselis *et al.* (2012) [79]. It was found that the threshold fluence decreased with increasing beam diameter. It was

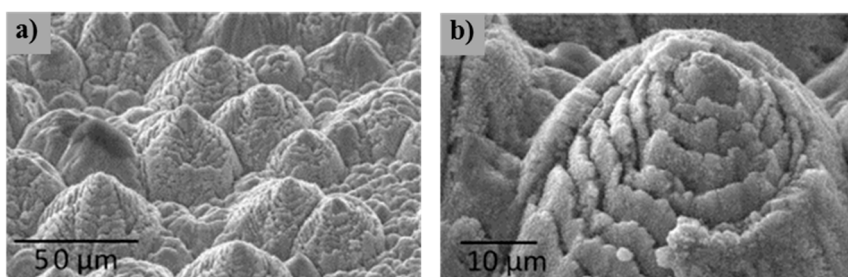
suggested that the planar plasma expansion at larger beam diameters is responsible for this behaviour. The effect of backpressure was also studied: higher backpressure proved to be more favourable for columnar structure formation. Kurselis *et al.* (2012) argued that at threshold fluence for columnar structure formation the plasma-surface interaction becomes dominant and plasma-etching effects are important. Plasma etching is more effective when the backpressure is higher which thus explains the observed phenomenon. Table 5 presents the characteristic sizes and associated fluence for columnar structures on different metals and alloys.

Pyramid structure. The columnar structures discussed in the previous section have an aspect ratio of 2:1 or higher. In contrast, Zuhlke *et al.* (2013) observed another surface morphology close to the threshold fluence that has an aspect ratio of 1:1. This surface structure was named nanoparticle covered pyramid (NC pyramid) because the pyramid-like structure was covered by a thick layer of nanoparticles [30]. Figure 8 shows the NC pyramid structure on Ni. Energy-dispersive X-ray spectroscopy (EDX) and transmission electron microscopy (TEM) analysis conducted on columnar and NC pyramid structures revealed that the core of the structure for both cases was pure metal (Ni in this specific case). However, deposited nanoparticles were oxides of the metal. It was also observed that the columnar structures were made of multiple grains, whereas NC pyramids were made of a single grain [124].

Table 5. Characteristics of columnar structures on different metals and alloys. * Values are estimated from the SEM images. ** The authors reported peak fluence value. n.s. = not specified.

Metals and Alloys	Size (µm)	Height (µm)	Fluence (J/cm ²)	Reference
	1–6 *	n.s.	0.75	[29]
	1–15	n.s.	0.16–0.35	[84]
	>10	15	1.5–2.5	[123]
Ti	2–3	n.s.	3.3–9.9 (in water)	[10]
	10	n.s.	1	[111]
	5–10	15–20	1.2	[117]
Ti-6-4	12	12	5.16	[115]
AISI 304L	9	9	5.16	[115]
AISI 316L	6–8	5–11	0.8–1.6 (in vacuum)	[114]
	<50	n.s.	1	[120]
	n.s.	n.s.	21	[121]
Al	30	40–70	13.5 **	[5]
	3–10 *	n.s.	0.16	[117]
Ni	5–15 *	n.s.	1.392–3.08	[87]

Figure 8. (a) NC pyramid on Ni, (b) magnified view showing the layered nanoparticle clusters [30].



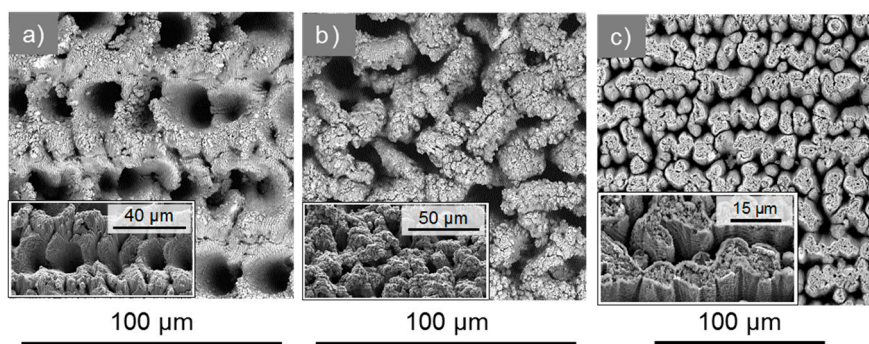
3.2.3. Other Structures

Hole Structures. It is possible to ablate a hole smaller than the beam spot size if only the center of the Gaussian beam is above the ablation threshold of the material. Pronko *et al.* (1995) fabricated a 300 nm hole by a 3 μm spot size beam on Ag with a 200 fs pulsed Ti:sapphire laser [32]. Perrie *et al.* (2004) ablated Al in a He environment with a beam diameter of 30 μm in a raster scan pattern, and observed microholes throughout the scanned area [73]. The holes were irregular in size and arrangements, and their diameters were up to ~ 15 μm . Nayak and Gupta (2010) ablated a Ti foil at 1.2 J/cm^2 and 1000 pulses per spot to generate random hole patterns [117]. The size of the holes varied from a few micrometers to a few hundred nanometers. More regular hole patterns were observed on Ti, SS304, and SS316 at a fluence higher than the fluence level needed for columnar structure formation [48,81,84,114]. Regular hole structures on Ti are shown in Figure 9a. The features are flared at the top for the hole structures, unlike the round or conical shape of the columnar structures. The size of the holes is less than the effective beam diameter. The formation of hole structures was found to be highly influenced by the surface inhomogeneities and pre-produced roughness [79]. Thus, position and size of such features can be easily controlled. These hole structures are the precursors for the chaotic and rugged structures, which are discussed in the following section.

Chaotic and rugged structures. Chaotic and rugged structures were observed on Ti, SS304, SS316, and Cu [71,81]. It was observed that high fluences and high line overlap favour rugged-chaotic structures. Moradi *et al.* (2013) referred to these structures as triple roughness structures. The presence of LIPSS was difficult to verify on these structures. An example of such rugged-chaotic structures is shown in Figure 9b. Higher fluence does not always create rough surface structures, particularly at low number of pulses. In one such experiment, at very high laser fluence (2.9 J/cm^2) and only with a single pulse, titanium melted, and a smooth surface with few inhomogeneities was left behind [84].

Others. Within our previous work we have observed a maze-like structure on Al at a fluence lower than the regular columnar structure formation fluence [48]. Such maze-like structures are shown in Figure 9c. We have further classified other surface structures, for example, trench structures and nano-forest structures on Cu.

Figure 9. (a) Hole structure on Ti. Inset: high magnification image of sample tilted at an angle of 25°. (b) Chaotic and rugged structure on Ti. Inset: high magnification image of sample tilted at an angle of 40°. (c) Maze structure on Al. Inset: high magnification image of sample tilted at an angle of 25° [48].



4. Laser-Inscribed Surface Structures

The laser-induced structures discussed so far are also termed as self-organized surface structures in laser processing. We want to emphasize here that the self-organization in laser micromachining process is characterized by structures of dimensions smaller than the size of the effective laser beam diameter [12,79,87,89,109,117]. The feature sizes of the laser-inscribed surface structures are approximately equal to or larger than the effective beam diameter. These structures are useful for various applications, such as microfluidics and those related to the altered wetting behaviours. We have created laser-inscribed surface structures, such as square pillars, parallel grooves, pyramids, columns and hole structures on copper (99.9% pure, McMaster-Carr), with a Ti:sapphire (<100 fs pulse duration, 800 nm wavelength, and 10 kHz repetition rate) laser. Figures 10 and 11 show the SEM images of different regular patterns on Cu. All the structures have hierarchical features as shown in SEM micrographs.

Figure 10. SEM micrographs of: (a) pyramid structures and (b) column structures on Cu. Inset: magnified view showing the hierarchical nature of the structures.

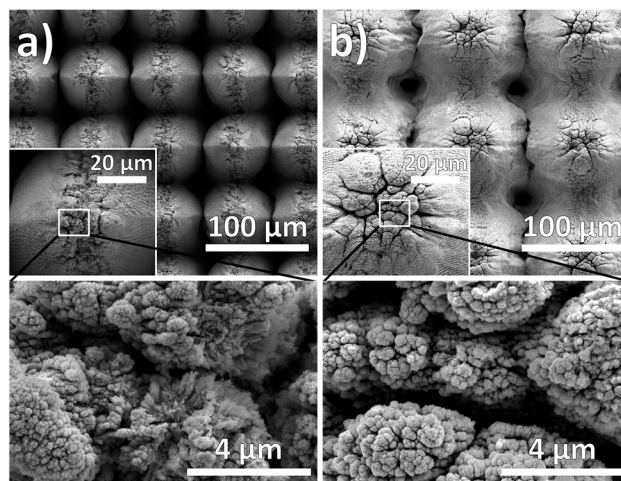
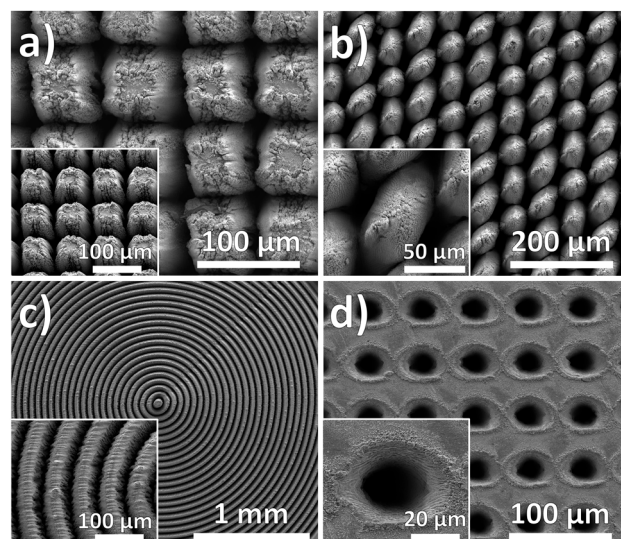


Figure 11. SEM micrographs of: (a) square pillar, inset: sample tilted at 20° angle; (b) parallelogram structures in a hexagonal arrangement, inset: zoomed in view; (c) circular grooves, inset: zoomed in view; and (d) micro hole pattern on Cu, inset: zoomed in view.



Other researchers have studied laser-inscribed surface structures in recent years. The types of structures in this case are limited only by human imagination. Parallel microgroove patterns on Pt were reported by Vorobyev *et al.* (2008) [125]. Parallel microgroove patterns on silicon and glass were also reported in literature [126,127]. Li *et al.* (2008) [128] fabricated square pillar structures on Ti with a 70 μm diameter fs laser beam. The sides of these square pillars were designed to be 30 μm , whereas the distance between the pillars varied from 70 to 130 μm . In the studies described above, the pillar/groove structures were decorated with sub-micron and microstructures. Moreover, because of the asymmetric energy distribution of the Gaussian beam, the sidewalls were not vertical. Wang *et al.* (2008) investigated the effect of sample distance from the lens; they observed that a microgroove ablated by a convergent beam had a V-shape whereas the groove ablated by the divergent beam had a U-shape [129]. They also observed that the position of the sample altered the morphology of the structures. Ablation with divergent beam leaves redeposited material throughout the ablated region because of the effect of the plasma at the focal plane above the machining plane.

5. Structure Optimization

Different surface structures can be achieved by tuning one or more of the parameters stated in Section 2.2. All these parameters ultimately affect the total amount of laser energy reaching the surface, as well as the spatial and temporal profile of this energy. We have previously proposed two different models for structure optimization: Accumulated Fluence Profile (AFP) and Fluence-Pulse Per Spot (F-PPS) [48]. These two models include the pulse energy, repetition rate of the laser beam, beam diameter, scanning velocity, and overlap, which are expressed by two new parameters that enable direct structure optimization. The Pulse Per Spot is defined as:

$$\text{PPS}_{tot} = (\text{PPS}_x) (\text{PPS}_z) = \left(\frac{\omega_0}{\Delta x}\right) \left(\frac{\omega_0}{\Delta z}\right) \quad (13)$$

where $\Delta x = \frac{v}{f}$. Peak fluence is used for the F-PPS model. An irradiation model developed by Eichstädt *et al.* (2013) was used for the AFP model to calculate the total fluence distribution over a reference area by summing individual Gaussian pulses displaced by Δx and Δz [130]. The spatial distribution of fluence for each pulse is given by:

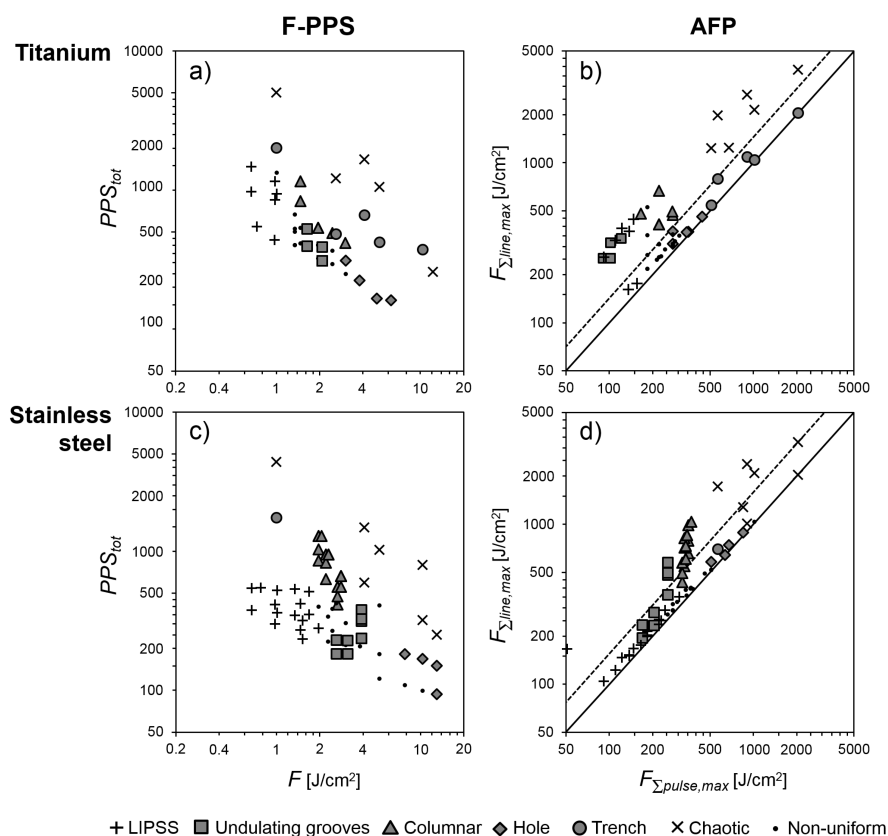
$$F_p(x, y, z) = \left(\frac{8P}{\pi\omega_0^2 f}\right) \exp\left(-\frac{8(x^2+z^2)}{\omega_0^2}\right) \quad (14)$$

Successive pulses in Δx displacement are summed up to give the pulse-accumulated fluence, $F_{\Sigma pulse}$, whereas overlapping the pulse-accumulated fluence in Δz displacement leads to the line-accumulated fluence, $F_{\Sigma line}$. Two important assumptions for this model are: (1) the sample displacement is negligible compared to the pulse duration of the laser beam, and (2) the spatial fluence profile is flat for pulse-accumulated fluence.

The comparison of different surface structures formation on Ti and SS304 are presented in Figure 12 in terms of two calculated parameters for both models. These two models can differentiate between different structures by narrowing down the experimental space. For example, if the objective of micromachining is to fabricate a columnar structure and the settings for undulating grooves are known, then it is easy to make a decision about which experimental parameters should be changed for fabricating the columnar structures. According to Figure 12, it is possible to fabricate columnar structure by

lowering the fluence and increasing the PPS for F-PPS model. Fluence can be decreased by decreasing the power of the laser beam or moving the sample away from the focal plane. PPS can be increased by lowering the scan velocity or increasing the line-overlap. In addition, the AFP model provides further information, such as whether to lower the scan velocity or increase the line-overlap to get the desired results. For more details regarding these two models the reader is referred to [48].

Figure 12. Micromachining parameters for different surface structures in terms of two parameters for F-PPS and AFP model [48]. The dashed line indicates the transition from wavy-to-flat $F_{\Sigma line}$ profile.



6. Applications

The surface structures so far described in previous sections can find various applications, as already tested by many researchers. Many other applications are considered but not tested. The main applications of these surfaces range from the modification of wetting behaviour over biomedical applications to the modification of light absorption. The discussion that follows incorporates both metals and other materials to give a broader view of the applications of fs laser textured surfaces.

Most often, the creation of superhydrophobic surfaces is the desired outcome when modifying the wetting properties of surfaces. Large varieties of nano- and microstructures that result in superhydrophobic surfaces have been created on metal surfaces by fs laser micromachining, mostly on stainless steel [81,114,115]. Generally, surface chemistry or surface structures alone are not capable to show superhydrophobic behaviour. Surface chemistry and surface structures both contribute toward the superhydrophobicity of a surface. Especially, dual-scale structures containing both nano- and microscale features lead to robust superhydrophobic surface and increased contact angles [114]. Moreover, Kietzig *et al.* (2009) noted that

it takes some time for superhydrophobicity to develop on intrinsically hydrophilic metals, which they attributed to the formation of a carbonaceous surface layer after laser treatment that alters the chemistry of the surface [115]. Superhydrophobicity is also possible on silicon surfaces, which are patterned with hierarchical cone structures by a femtosecond laser [7,131]. In general, such superhydrophobic surfaces have various applications including self-cleaning and drag reduction in fluid flow. In addition to creating superhydrophobic surfaces, parallel microgroove patterns favour rapid uphill transport of liquids, such as methanol, through capillarity [8]. Apart from fabricating superhydrophobic surfaces, fs laser textured surfaces can also be used to fabricate hydrophilic surfaces, which can be used for fluid separation in microchannels [132,133]. Furthermore, it is possible to create structures with enhanced frictional properties, which can be beneficial for the winter sport industry [6]. Finally, laser-inscribed structures can reduce the wear in mechanical parts [20,134] as well as can act as lubricant reservoirs and capture wear debris in the pits [135,136].

A vast array of biomedical applications exist, most of which are concerned with the microstructuring and biointegration of implant materials. Several research studies report that the creation of nano- and microstructures on titanium implant material using femtosecond lasers increases the adhesion of osteoblasts while hindering the attachment of fibroblasts, which is desired in implant materials, as it promotes better bone integration [10,11,84,137]. These studies generally correlate the improved osseointegration with superhydrophobic surface structures, which suggests that the wetting behaviour may be suitable to determine cell response on patterned surfaces [138]. While titanium is a popular material for biomedical implants, several other materials, such as stainless steel [139], titanium/niobium/zirconium alloys [140], nickel/titanium alloy [9], platinum [138], and silicon [141], have been investigated and shown to result in similarly beneficial properties for biocompatibility. Apart from osteoblasts and fibroblasts, selective proliferation of neurons was demonstrated on a silicon surface microstructured by a femtosecond laser [142]. Another study involved creating superhydrophilic human enamel and dentin with a femtosecond laser to enhance adhesion in dentistry applications, since chemically modifying the surface would be a complicated procedure [143].

Even applications concerning the aesthetic component of the laser-treated surfaces are conceivable. These include modifying the color of metal surfaces. The presence of nano- and microstructures generally leads to an altered light absorption behaviour, which often results in surfaces that appear dark gray or black and are highly absorptive [70,125]. By finely tuning the surface structures, it is possible to create structurally coloured metal surfaces, the absorption properties of which can be controlled over the ultraviolet to terahertz range [1,144]. Furthermore, the optical properties can be tuned to create metals exhibiting different colors at different viewing angles [145,146]. As a culmination of these phenomena, a complete “painting” was created solely by controlling the nanostructures obtained using a femtosecond laser [147]. The absorptive properties of femtosecond laser treated surfaces are also promising for use in solar cell applications [4,148] as they enhance absorption in the ultraviolet region while maintaining low emissivity in the infrared region [3].

There are several other active areas of research concerned with the applications of femtosecond laser treated surfaces. These include improving the performance of silicon photodiodes [16,17,149] and enhancing the X-ray generation of iron surfaces [19]. Furthermore, the thermal emissivity of metals can be greatly increased, which is promising for the creation of brighter and more efficient light sources [15,150]. Lastly, an unconventional technique has been explored to create stainless steel micro-moulds by using a

combination of femtosecond laser cutting and micro-electric resistance slip welding to create high precision moulds [151].

7. Conclusions

It is possible to fabricate many different surface structures on different metals and alloys by femtosecond laser micromachining. Though the formation of laser-irradiated surface structures is complex, many formation mechanisms have been proposed and experimentally tested to advance our understanding. However, the complete picture of surface structure formation is still outstanding, and more research work is needed to better describe structure formation. Different parameters for fs laser texturing have been identified, and their effect on surface texturing has been discussed in this review. An optimization tool for fine-tuning of the structures has also been presented. Finally, we have shown that the prospect of the application of these surface structures is tremendous, and fs laser micromachining can be a suitable process for industrial use.

Acknowledgements

The authors gratefully acknowledge the National Science and Research Council of Canada (NSERC) and Fonds de Recherche du Québec-Nature et Technologies (FRQNT) for their financial support of this work.

Author Contributions

K. M. Tanvir Ahmmed wrote the manuscript, conceptualized and supervised the laser-inscribed experiments, and carried out the scanning electron microscopy. Colin Grambow designed and performed the laser-inscribed experiments and edited the manuscript. Anne-Marie Kietzig supervised the work and edited the manuscript.

Conflicts of Interest

The authors declare no conflict of interest.

References

1. Vorobyev, A.Y.; Guo, C.L. Metal colorization with femtosecond laser pulses. In Proceedings of SPIE on High-Power Laser Ablation VII, Taos, NM, USA, 20–24 April 2008.
2. Yao, J.W.; Zhang, C.Y.; Liu, H.Y.; Dai, Q.F.; Wu, L.J.; Lan, S.; Gopal, A.V.; Trofimov, V.A.; Lysak, T.M. Selective appearance of several laser-induced periodic surface structure patterns on a metal surface using structural colors produced by femtosecond laser pulses. *Appl. Surf. Sci.* **2012**, *258*, 7625–7632.
3. Hwang, T.Y.; Vorobyev, A.Y.; Guo, C.L. Enhanced efficiency of solar-driven thermoelectric generator with femtosecond laser-textured metals. *Opt. Expr.* **2011**, *19*, A824–A829.
4. Nayak, B.K.; Iyengar, V.V.; Gupta, M.C. Efficient light trapping in silicon solar cells by ultrafast-laser-induced self-assembled micro/nano structures. *Prog. Photovolt. Res. Appl.* **2011**, *19*, 631–639.

5. Singh, N.; Alexander, D.R.; Schiffern, J.; Doerr, D. Femtosecond laser production of metal surfaces having unique surface structures that are broadband absorbers. *J. Laser Appl.* **2006**, *18*, 242–244.
6. Kietzig, A.M.; Hatzikiriakos, S.G.; Englezos, P. Ice friction: The effects of surface roughness, structure, and hydrophobicity. *J. Appl. Phys.* **2009**, *106*, 024303.
7. Zorba, V.; Stratakis, E.; Barberoglou, M.; Spanakis, E.; Tzanetakis, P.; Anastasiadis, S.H.; Fotakis, C. Biomimetic artificial surfaces quantitatively reproduce the water repellency of a lotus leaf. *Adv. Mater.* **2008**, *20*, 4049–4054.
8. Vorobyev, A.Y.; Guo, C.L. Metal pumps liquid uphill. *Appl. Phys. Lett.* **2009**, *94*, 224102.
9. Liang, C.Y.; Wang, H.S.; Yang, J.J.; Li, B.; Yang, Y.; Li, H.P. Biocompatibility of the micro-patterned NiTi surface produced by femtosecond laser. *Appl. Surf. Sci.* **2012**, *261*, 337–342.
10. Yang, Y.; Yang, J.J.; Liang, C.Y.; Wang, H.S.; Zhu, X.N.; Zhang, N. Surface microstructuring of Ti plates by femtosecond lasers in liquid ambiances: A new approach to improving biocompatibility. *Opt. Expr.* **2009**, *17*, 21124–21133.
11. Fadeeva, E.; Schlie, S.; Koch, J.; Chichkov, B.N. Selective cell control by surface structuring for orthopedic applications. *J. Adhes. Sci. Technol.* **2010**, *24*, 2257–2270.
12. Fadeeva, E.; Truong, V.K.; Stiesch, M.; Chichkov, B.N.; Crawford, R.J.; Wang, J.; Ivanova, E.P. Bacterial retention on superhydrophobic titanium surfaces fabricated by femtosecond laser ablation. *Langmuir* **2011**, *27*, 3012–3019.
13. Liang, F.; Lehr, J.; Danielczak, L.; Leask, R.; Kietzig, A.M. Robust non-wetting PTFE surfaces by femtosecond laser machining. *Int. J. Mol. Sci.* **2014**, *15*, 13681–13696.
14. Truong, S.L.; Levi, G.; Bozon-Verduraz, F.; Petrovskaya, A.V.; Simakin, A.V.; Shafeev, G.A. Generation of nanospikes via laser ablation of metals in liquid environment and their activity in surface-enhanced raman scattering of organic molecules. *Appl. Surf. Sci.* **2007**, *254*, 1236–1239.
15. Yang, J.; Yang, Y.; Zhao, B.; Wang, Y.; Zhu, X. Femtosecond laser-induced surface structures to significantly improve the thermal emission of light from metals. *Appl. Phys. B Lasers Opt.* **2012**, *106*, 349–355.
16. Carey, J.E.; Crouch, C.H.; Shen, M.Y.; Mazur, E. Visible and near-infrared responsivity of femtosecond-laser microstructured silicon photodiodes. *Opt. Lett.* **2005**, *30*, 1773–1775.
17. Myers, R.A.; Farrell, R.; Karger, A.M.; Carey, J.E.; Mazur, E. Enhancing near-infrared avalanche photodiode performance by femtosecond laser microstructuring. *Appl. Opt.* **2006**, *45*, 8825–8831.
18. Barmina, E.V.; Barberoglou, M.; Zorba, V.; Simakin, A.V.; Stratakis, E.; Fotakis, C.; Shafeev, G.A. Laser control of the properties of nanostructures on Ta and Ni under their ablation in liquids. *J. Optoelectron. Adv. Mater.* **2010**, *12*, 495–499.
19. Volkov, R.V.; Golishnikov, D.M.; Gordienko, V.M.; Savel'ev, A.B. Overheated plasma at the surface of a target with a periodic structure induced by femtosecond laser radiation. *JETP Lett.* **2003**, *77*, 473–476.
20. Wan, Y.; Xiong, D.-S. The effect of laser surface texturing on frictional performance of face seal. *J. Mater. Process. Technol.* **2008**, *197*, 96–100.
21. Hecht, J. A short history of laser development. *Appl. Opt.* **2010**, *49*, F99–F122.
22. Fork, R.L.; Greene, B.I.; Shank, C.V. Generation of optical pulses shorter than 0.1 psec by colliding pulse mode locking. *Appl. Phys. Lett.* **1981**, *38*, 671–672.
23. Maiman, T.H. Stimulated optical radiation in ruby. *Nature* **1960**, *187*, 493–494.

24. Nisoli, M.; DeSilvestri, S.; Svelto, O.; Szipocs, R.; Ferencz, K.; Spielmann, C.; Sartania, S.; Krausz, F. Compression of high-energy laser pulses below 5 fs. *Opt. Lett.* **1997**, *22*, 522–524.
25. Zhao, K.; Zhang, Q.; Chini, M.; Wu, Y.; Wang, X.; Chang, Z. Tailoring a 67 attosecond pulse through advantageous phase-mismatch. *Opt. Lett.* **2012**, *37*, 3891–3893.
26. Birnbaum, M. Semiconductor surface damage produced by ruby lasers. *J. Appl. Phys.* **1965**, *36*, 3688–3689.
27. Kautek, W.; Kruger, J. Femtosecond pulse laser-ablation of metallic, semiconducting, ceramic, and biological-materials. In Proceeding of SPIE 2207 Laser Materials Processing: Industrial and Microelectronics Applications, Vienna, Austria, 5–8 April 1994.
28. Herbst, G.; Steiner, M.; Marowsky, G.; Matthias, E. Ablation of Si and Ge using UV femtosecond laser pulses. In Proceedings of Symposium on Advanced Laser Processing of Materials—Fundamentals and Applications at the 1995 MRS Fall Meeting, Boston, MA, USA, 27 November–1 December 1995; Volume 397, pp. 69–74.
29. Tsukamoto, M.; Asuka, K.; Nakano, H.; Hashida, M.; Katto, M.; Abe, N.; Fujita, M. Periodic microstructures produced by femtosecond laser irradiation on titanium plate. *Vacuum* **2006**, *80*, 1346–1350.
30. Zuhlke, C.A.; Anderson, T.P.; Alexander, D.R. Fundamentals of layered nanoparticle covered pyramidal structures formed on nickel during femtosecond laser surface interactions. *Appl. Surf. Sci.* **2013**, *283*, 648–653.
31. Preuss, S.; Demchuk, A.; Stuke, M. Subpicosecond UV laser-ablation of metals. *Appl. Phys. A* **1995**, *61*, 33–37.
32. Pronko, P.P.; Dutta, S.K.; Squier, J.; Rudd, J.V.; Du, D.; Mourou, G. Machining of submicron holes using a femtosecond laser at 800-nm. *Opt. Commun.* **1995**, *114*, 106–110.
33. Chichkov, B.N.; Momma, C.; Nolte, S.; vonAlvensleben, F.; Tunnermann, A. Femtosecond, picosecond and nanosecond laser ablation of solids. *Appl. Phys. A* **1996**, *63*, 109–115.
34. Kanavin, A.P.; Smetanin, I.V.; Isakov, V.A.; Afanasiev, Y.V.; Chichkov, B.N.; Wellegehausen, B.; Nolte, S.; Momma, C.; Tunnermann, A. Heat transport in metals irradiated by ultrashort laser pulses. *Phys. Rev. B* **1998**, *57*, 14698–14703.
35. Nolte, S.; Momma, C.; Jacobs, H.; Tunnermann, A.; Chichkov, B.N.; Wellegehausen, B.; Welling, H. Ablation of metals by ultrashort laser pulses. *J. Opt. Soc. Am. B Opt. Phys.* **1997**, *14*, 2716–2722.
36. Liu, X.; Du, D.; Mourou, G. Laser ablation and micromachining with ultrashort laser pulses. *IEEE J. Quantum Electron.* **1997**, *33*, 1706–1716.
37. Valette, S.; Audouard, E.; Le Harzic, R.; Huot, N.; Laporte, P.; Fortunier, R. Heat affected zone in aluminum single crystals submitted to femtosecond laser irradiations. *Appl. Surf. Sci.* **2005**, *239*, 381–386.
38. Joglekar, A.P.; Liu, H.; Spooner, G.J.; Meyhofer, E.; Mourou, G.; Hunt, A.J. A study of the deterministic character of optical damage by femtosecond laser pulses and applications to nanomachining. *Appl. Phys. B Lasers Opt.* **2003**, *77*, 25–30.
39. Chimmalgi, A.; Choi, T.Y.; Grigoropoulos, C.P.; Komvopoulos, K. Femtosecond laser aperturless near-field nanomachining of metals assisted by scanning probe microscopy. *Appl. Phys. Lett.* **2003**, *82*, 1146–1148.

40. Momma, C.; Nolte, S.; Chichkov, B.N.; von Alvensleben, F.; Tunnermann, A. Precise laser ablation with ultrashort pulses. *Appl. Surf. Sci.* **1997**, *109*, 15–19.
41. Arrigoni, M. Femtosecond lasers carve out a niche in micromachining. *Photon. Spectra* **2004**, *38*, 73.
42. Schaffer, C.B.; Brodeur, A.; Mazur, E. Laser-induced breakdown and damage in bulk transparent materials induced by tightly focused femtosecond laser pulses. *Meas. Sci. Technol.* **2001**, *12*, 1784–1794.
43. Wang, C.; Chang, Y.C.; Yao, J.M.; Luo, C.R.; Yin, S.; Ruffin, P.; Brantley, C.; Edwards, E. Surface enhanced raman spectroscopy by interfered femtosecond laser created nanostructures. *Appl. Phys. Lett.* **2012**, *100*, 023107.
44. Kietzig, A.M.; Lehr, J.; Matus, L.; Liang, F. Laser-induced patterns on metals and polymers for biomimetic surface engineering. In Proceedings of SPIE 8967 Laser Applications in Microelectronic and Optoelectronic Manufacturing XIX, San Francisco, CA, USA, 1 February 2014.
45. Murray, M.; Jose, G.; Richards, B.; Jha, A. Femtosecond pulsed laser deposition of silicon thin films. *Nanoscale Res. Lett.* **2013**, *8*, 272.
46. Anisimov, S.I.; Kapeliov, B.L.; Perelman, T.L. Electron-emission from surface of metals induced by ultrashort laser pulses. *Zh. Eksp. Teor. Fiz.* **1974**, *66*, 776–781.
47. Von der Linde, D.; Sokolowski-Tinten, K.; Bialkowski, J. Laser-solid interaction in the femtosecond time regime. *Appl. Surf. Sci.* **1997**, *109*, 1–10.
48. Ahmmed, K.M.T.; Ling, E.J.Y.; Servio, P.; Kietzig, A.-M. Introducing a new optimization tool for femtosecond laser-induced surface texturing on titanium, stainless steel, aluminum and copper. *Opt. Lasers Eng.* **2015**, *66*, 258–268.
49. Miotello, A.; Kelly, R. Laser-induced phase explosion: New physical problems when a condensed phase approaches the thermodynamic critical temperature. *Appl. Phys. A* **1999**, *69*, S67–S73.
50. Cheng, C.R.; Xu, X.F. Mechanisms of decomposition of metal during femtosecond laser ablation. *Phys. Rev. B* **2005**, *72*, 165415.
51. Bouilly, D.; Perez, D.; Lewis, L.J. Damage in materials following ablation by ultrashort laser pulses: A molecular-dynamics study. *Phys. Rev. B* **2007**, *76*, 184119.
52. Perez, D.; Lewis, L.J. Molecular-dynamics study of ablation of solids under femtosecond laser pulses. *Phys. Rev. B* **2003**, *67*, 184102.
53. Ivanov, D.S.; Zhigilei, L.V. Combined atomistic-continuum modeling of short-pulse laser melting and disintegration of metal films. *Phys. Rev. B* **2003**, *68*, 064114.
54. Stoian, R.; Ashkenasi, D.; Rosenfeld, A.; Campbell, E.E.B. Coulomb explosion in ultrashort pulsed laser ablation of Al₂O₃. *Phys. Rev. B* **2000**, *62*, 13167–13173.
55. Shirk, M.D.; Molian, P.A. A review of ultrashort pulsed laser ablation of materials. *J. Laser Appl.* **1998**, *10*, 18–28.
56. Cheng, J.; Liu, C.-S.; Shang, S.; Liu, D.; Perrie, W.; Dearden, G.; Watkins, K. A review of ultrafast laser materials micromachining. *Opt. Laser Technol.* **2013**, *46*, 88–102.
57. Kruger, J.; Kautek, W. Ultrashort pulse laser interaction with dielectrics and polymers. *Adv. Polym. Sci.* **2004**, *168*, 247–289.
58. Mannion, P.T.; Magee, J.; Coyne, E.; O'Connor, G.M.; Glynn, T.J. The effect of damage accumulation behaviour on ablation thresholds and damage morphology in ultrafast laser micro-machining of common metals in air. *Appl. Surf. Sci.* **2004**, *233*, 275–287.

59. Jee, Y.; Becker, M.F.; Walser, R.M. Laser-induced damage on single-crystal metal-surfaces. *J. Opt. Soc. Am. B Opt. Phys.* **1988**, *5*, 648–659.
60. Semaltianos, N.G.; Perrie, W.; French, P.; Sharp, M.; Dearden, G.; Logothetidis, S.; Watkins, K.G. Femtosecond laser ablation characteristics of nickel-based superalloy C263. *Appl. Phys. A* **2009**, *94*, 999–1009.
61. Rosenfeld, A.; Lorenz, M.; Stoian, R.; Ashkenasi, D. Ultrashort-laser-pulse damage threshold of transparent materials and the role of incubation. *Appl. Phys. A* **1999**, *69*, S373–S376.
62. Gamaly, E.G.; Madsen, N.R.; Duering, M.; Rode, A.V.; Kolev, V.Z.; Luther-Davies, B. Ablation of metals with picosecond laser pulses: Evidence of long-lived nonequilibrium conditions at the surface. *Phys. Rev. B* **2005**, *71*, 174405.
63. Gamaly, E.G.; Rode, A.V.; Luther-Davies, B.; Tikhonchuk, V.T. Ablation of solids by femtosecond lasers: Ablation mechanism and ablation thresholds for metals and dielectrics. *Phys. Plasmas* **2002**, *9*, 949–957.
64. Wellershoff, S.S.; Hohlfeld, J.; Gudde, J.; Matthias, E. The role of electron-phonon coupling in femtosecond laser damage of metals. *Appl. Phys. A* **1999**, *69*, S99–S107.
65. Stuart, B.C.; Feit, M.D.; Herman, S.; Rubenchik, A.M.; Shore, B.W.; Perry, M.D. Optical ablation by high-power short-pulse lasers. *J. Opt. Soc. Am. B Opt. Phys.* **1996**, *13*, 459–468.
66. Gudde, J.; Hohlfeld, J.; Muller, J.G.; Matthias, E. Damage threshold dependence on electron-phonon coupling in Au and Ni films. *Appl. Surf. Sci.* **1998**, *127*, 40–45.
67. Yahng, J.S.; Nam, J.R.; Jeoung, S.C. The influence of substrate temperature on femtosecond laser micro-processing of silicon, stainless steel and glass. *Opt. Lasers Eng.* **2009**, *47*, 815–820.
68. Vorobyev, A.Y.; Guo, C.L. Femtosecond laser nanostructuring of metals. *Opt. Expr.* **2006**, *14*, 2164–2169.
69. Kruger, J.; Kautek, W. The femtosecond pulse laser: A new tool for micromachining. *Laser Phys.* **1999**, *9*, 30–40.
70. Vorobyev, A.Y.; Guo, C. Enhanced absorptance of gold following multipulse femtosecond laser ablation. *Phys. Rev. B* **2005**, *72*, 195422.
71. Groenendijk, M.; Meijer, J. Microstructuring using femtosecond pulsed laser ablation. *J. Laser Appl.* **2006**, *18*, 227–235.
72. Martin, S.; Kruger, J.; Hertwig, A.; Fiedler, A.; Kautek, W. Femtosecond laser interaction with protection materials. *Appl. Surf. Sci.* **2003**, *208*, 333–339.
73. Perrie, W.; Gill, M.; Robinson, G.; Fox, P.; O'Neill, W. Femtosecond laser micro-structuring of aluminium under helium. *Appl. Surf. Sci.* **2004**, *230*, 50–59.
74. Will, M.; Nolte, S.; Chichkov, B.N.; Tunnermann, A. Optical properties of waveguides fabricated in fused silica by femtosecond laser pulses. *Appl. Opt.* **2002**, *41*, 4360–4364.
75. Noh, J.; Lee, J.H.; Na, S.; Lim, H.; Jung, D.H. Fabrication of hierarchically micro- and nano-structured mold surfaces using laser ablation for mass production of superhydrophobic surfaces. *Jpn. J. Appl. Phys.* **2010**, *49*, 106502.
76. Hall, D.G. Vector-beam solutions of Maxwell's wave equation. *Opt. Lett.* **1996**, *21*, 9–11.
77. Semaltianos, N.G.; Perrie, W.; French, P.; Sharp, M.; Dearden, G.; Watkins, K.G. Femtosecond laser surface texturing of a nickel-based superalloy. *Appl. Surf. Sci.* **2008**, *255*, 2796–2802.

78. Bizi-Bandoki, P.; Benayoun, S.; Valette, S.; Beaugiraud, B.; Audouard, E. Modifications of roughness and wettability properties of metals induced by femtosecond laser treatment. *Appl. Surf. Sci.* **2011**, *257*, 5213–5218.
79. Kurselis, K.; Kiyan, R.; Chichkov, B.N. Formation of corrugated and porous steel surfaces by femtosecond laser irradiation. *Appl. Surf. Sci.* **2012**, *258*, 8845–8852.
80. Bonse, J.; Kruger, J.; Hohm, S.; Rosenfeld, A. Femtosecond laser-induced periodic surface structures. *J. Laser Appl.* **2012**, *24*, 042006.
81. Moradi, S.; Kamal, S.; Englezos, P.; Hatzikiriakos, S.G. Femtosecond laser irradiation of metallic surfaces: Effects of laser parameters on superhydrophobicity. *Nanotechnology* **2013**, *24*, 415302.
82. Bizi-bandoki, P.; Valette, S.; Audouard, E.; Benayoun, S. Effect of stationary femtosecond laser irradiation on substructures' formation on a mold stainless steel surface. *Appl. Surf. Sci.* **2013**, *270*, 197–204.
83. Lehr, J.; Kietzig, A.-M. Production of homogenous micro-structures by femtosecond laser micro-machining. *Opt. Lasers Eng.* **2014**, *57*, 121–129.
84. Vorobyev, A.Y.; Guo, C. Femtosecond laser structuring of titanium implants. *Appl. Surf. Sci.* **2007**, *253*, 7272–7280.
85. Vorobyev, A.Y.; Guo, C.L. Direct femtosecond laser surface nano/microstructuring and its applications. *Laser Photonics Rev.* **2013**, *7*, 385–407.
86. Tsibidis, G.D.; Barberoglou, M.; Loukakos, P.A.; Stratakis, E.; Fotakis, C. Dynamics of ripple formation on silicon surfaces by ultrashort laser pulses in subablation conditions. *Phys. Rev. B* **2012**, *86*, 115316.
87. Zuhlke, C.A.; Anderson, T.P.; Alexander, D.R. Formation of multiscale surface structures on nickel via above surface growth and below surface growth mechanisms using femtosecond laser pulses. *Opt. Express* **2013**, *21*, 8460–8473.
88. Stratakis, E.; Zorba, V.; Barberoglou, M.; Fotakis, C.; Shafeev, G.A. Laser writing of nanostructures on bulk Al via its ablation in liquids. *Nanotechnology* **2009**, *20*, 105303.
89. Stratakis, E.; Zorba, V.; Barberoglou, M.; Fotakis, C.; Shafeev, G.A. Femtosecond laser writing of nanostructures on bulk Al via its ablation in air and liquids. *Appl. Surf. Sci.* **2009**, *255*, 5346–5350.
90. Dou, K.; Knobbe, E.T.; Parkhill, R.L.; Irwin, B.; Matthews, L.; Church, K.H. Femtosecond study of surface structure and composition and time-resolved spectroscopy in metals. *Appl. Phys. A* **2003**, *76*, 303–307.
91. Li, X.H.; Yuan, C.H.; Yang, H.D.; Li, J.W.; Huang, W.H.; Tang, D.C.; Xu, Q. Morphology and composition on Al surface irradiated by femtosecond laser pulses. *Appl. Surf. Sci.* **2010**, *256*, 4344–4349.
92. Barmina, E.V.; Stratakis, E.; Fotakis, K.; Shafeev, G.A. Generation of nanostructures on metals by laser ablation in liquids: New results. *Quantum Electron.* **2010**, *40*, 1012–1020.
93. Hwang, T.Y.; Vorobyev, A.Y.; Guo, C.L. Ultrafast dynamics of femtosecond laser-induced nanostructure formation on metals. *Appl. Phys. Lett.* **2009**, *95*, 123111.
94. Guosheng, Z.; Fauchet, P.M.; Siegman, A.E. Growth of spontaneous periodic surface-structures on solids during laser illumination. *Phys. Rev. B* **1982**, *26*, 5366–5381.
95. Young, J.F.; Preston, J.S.; Vandriel, H.M.; Sipe, J.E. Laser-induced periodic surface-structure. II. Experiments on Ge, Si, Al, and brass. *Phys. Rev. B* **1983**, *27*, 1155–1172.

96. Sipe, J.E.; Young, J.F.; Preston, J.S.; Vandriel, H.M. Laser-induced periodic surface-structure. 1. Theory. *Phys. Rev. B* **1983**, *27*, 1141–1154.
97. Reif, J.; Costache, F.; Henyk, M.; Pandelov, S.V. Ripples revisited: Non-classical morphology at the bottom of femtosecond laser ablation craters in transparent dielectrics. *Appl. Surf. Sci.* **2002**, *197–198*, 891–895.
98. Henyk, M.; Vogel, N.; Wolfframm, D.; Tempel, A.; Reif, J. Femtosecond laser ablation from dielectric materials: Comparison to arc discharge erosion. *Appl. Phys. A* **1999**, *69*, S355–S358.
99. Borowiec, A.; Haugen, H.K. Subwavelength ripple formation on the surfaces of compound semiconductors irradiated with femtosecond laser pulses. *Appl. Phys. Lett.* **2003**, *82*, 4462–4464.
100. Huang, M.; Zhao, F.; Cheng, Y.; Xu, N.; Xu, Z. Origin of laser-induced near-subwavelength ripples: Interference between surface plasmons and incident laser. *ACS Nano* **2009**, *3*, 4062–4070.
101. Bonchbruevich, A.M.; Libenson, M.N.; Makin, V.S.; Trubaev, V.V. Surface electromagnetic-waves in optics. *Opt. Eng.* **1992**, *31*, 718–730.
102. Romer, G.R.B.E.; Huis in't Veld, A.J.; Meijer, J.; Groenendijk, M.N.W. On the formation of laser induced self-organizing nanostructures. *Cirp Ann. Manuf. Technol.* **2009**, *58*, 201–204.
103. Zhao, Q.Z.; Malzer, S.; Wang, L.J. Formation of subwavelength periodic structures on tungsten induced by ultrashort laser pulses. *Opt. Lett.* **2007**, *32*, 1932–1934.
104. Okamuro, K.; Hashida, M.; Miyasaka, Y.; Ikuta, Y.; Tokita, S.; Sakabe, S. Laser fluence dependence of periodic grating structures formed on metal surfaces under femtosecond laser pulse irradiation. *Phys. Rev. B* **2010**, *82*, 165417.
105. Vorobyev, A.Y.; Makin, V.S.; Guo, C.L. Periodic ordering of random surface nanostructures induced by femtosecond laser pulses on metals. *J. Appl. Phys.* **2007**, *101*, 034903.
106. Vorobyev, A.Y.; Guo, C.L. Femtosecond laser-induced periodic surface structure formation on tungsten. *J. Appl. Phys.* **2008**, *104*, 063523.
107. Guan, Y.C.; Zhou, W.; Li, Z.L.; Zheng, H.Y. Femtosecond laser-induced iridescent effect on AZ31B magnesium alloy surface. *J. Phys. D Appl. Phys.* **2013**, *46*, 425305.
108. Hwang, T.Y.; Guo, C.L. Angular effects of nanostructure-covered femtosecond laser induced periodic surface structures on metals. *J. Appl. Phys.* **2010**, *108*, 073523.
109. Nayak, B.K.; Gupta, M.C. Ultrafast laser-induced self-organized conical micro/nano surface structures and their origin. *Opt. Lasers Eng.* **2010**, *48*, 966–973.
110. Yao, J.W.; Zhang, C.Y.; Liu, H.Y.; Dai, Q.F.; Wu, L.J.; Lan, S.; Gopal, A.V.; Trofimov, V.A.; Lysak, T.M. High spatial frequency periodic structures induced on metal surface by femtosecond laser pulses. *Opt. Express* **2012**, *20*, 905–911.
111. Oliveira, V.; Ausset, S.; Vilar, R. Surface micro/nanostructuring of titanium under stationary and non-stationary femtosecond laser irradiation. *Appl. Surf. Sci.* **2009**, *255*, 7556–7560.
112. Vorobyev, A.Y.; Guoa, C.L. Colorizing metals with femtosecond laser pulses. *Appl. Phys. Lett.* **2008**, *92*, 041914.
113. Sakabe, S.; Hashida, M.; Tokita, S.; Namba, S.; Okamuro, K. Mechanism for self-formation of periodic grating structures on a metal surface by a femtosecond laser pulse. *Phys. Rev. B* **2009**, *79*, 033409.
114. Wu, B.; Zhou, M.; Li, J.; Ye, X.; Li, G.; Cai, L. Superhydrophobic surfaces fabricated by microstructuring of stainless steel using a femtosecond laser. *Appl. Surf. Sci.* **2009**, *256*, 61–66.

115. Kietzig, A.-M.; Hatzikiriakosa, S.G.; Englezosa, P. Patterned superhydrophobic metallic surfaces. *Langmuir* **2009**, *25*, 4821–4827.
116. Jia, W.; Peng, Z.N.; Wang, Z.J.; Ni, X.C.; Wang, C.Y. The effect of femtosecond laser micromachining on the surface characteristics and subsurface microstructure of amorphous FeCuNbSiB alloy. *Appl. Surf. Sci.* **2006**, *253*, 1299–1303.
117. Nayak, B.K.; Gupta, M.C. Self-organized micro/nano structures in metal surfaces by ultrafast laser irradiation. *Opt. Lasers Eng.* **2010**, *48*, 940–949.
118. Zuhlke, C.A.; Anderson, T.P.; Alexander, D.R. Understanding the formation of self-organized micro/nanostructures on metal surfaces from femtosecond laser ablation using stop-motion SEM imaging. In Proceedings of SPIE 8968, Laser-based Micro- and Nanoprocessing VIII, San Francisco, CA, USA, 1 February 2014.
119. Lehr, J.; de Marchi, F.; Matus, L.; MacLeod, J.; Rosei, F.; Kietzig, A.-M. The influence of the gas environment on morphology and chemical composition of surfaces micro-machined with a femtosecond laser. *Appl. Surf. Sci.* **2014**, *320*, 455–465.
120. Kam, D.H.; Bhattacharya, S.; Mazumder, J. Control of the wetting properties of an AISI 316L stainless steel surface by femtosecond laser-induced surface modification. *J. Micromech. Microeng.* **2012**, *22*, 105019.
121. Robinson, G.M.; Jackson, M.J. Femtosecond laser micromachining of aluminum surfaces under controlled gas atmospheres. *J. Mater. Eng. Perform.* **2006**, *15*, 155–160.
122. Hwang, T.Y.; Guo, C.L. Polarization and angular effects of femtosecond laser-induced conical microstructures on Ni. *J. Appl. Phys.* **2012**, *111*, 083518.
123. Nayak, B.K.; Gupta, M.C.; Kolasinski, K.W. Formation of nano-textured conical microstructures in titanium metal surface by femtosecond laser irradiation. *Appl. Phys. A* **2008**, *90*, 399–402.
124. Zuhlke, C.A.; Anderson, T.P.; Alexander, D.R. Comparison of the structural and chemical composition of two unique micro/nanostructures produced by femtosecond laser interactions on nickel. *Appl. Phys. Lett.* **2013**, *103*, 121603.
125. Vorobyev, A.Y.; Guo, C. Femtosecond laser blackening of platinum. *J. Appl. Phys.* **2008**, *104*, 053516.
126. Vorobyev, A.Y.; Guo, C.L. Laser turns silicon superwicking. *Opt. Express* **2010**, *18*, 6455–6460.
127. Vorobyev, A.Y.; Guo, C.L. Optical and wetting properties of femtosecond laser nanostructured materials. *J. Nano Res.* **2011**, *14*, 57–67.
128. Li, B.J.; Zhou, M.; Yuan, R.; Cai, L. Fabrication of titanium-based microstructured surfaces and study on their superhydrophobic stability. *J. Mater. Res.* **2008**, *23*, 2491–2499.
129. Wang, W.J.; Mei, X.S.; Jiang, G.D.; Lei, S.T.; Yang, C.J. Effect of two typical focus positions on microstructure shape and morphology in femtosecond laser multi-pulse ablation of metals. *Appl. Surf. Sci.* **2008**, *255*, 2303–2311.
130. Eichstädt, J.; Römer, G.R.B.E.; Huis in't Veld, A.J. Determination of irradiation parameters for laser-induced periodic surface structures. *Appl. Surf. Sci.* **2013**, *264*, 79–87.
131. Baldacchini, T.; Carey, J.E.; Zhou, M.; Mazur, E. Superhydrophobic surfaces prepared by microstructuring of silicon using a femtosecond laser. *Langmuir* **2006**, *22*, 4917–4919.
132. Wang, Z.K.; Zheng, H.Y.; Xia, H.M. Femtosecond laser-induced modification of surface wettability of PMMA for fluid separation in microchannels. *Microfluid. Nanofluid.* **2011**, *10*, 225–229.

133. Chang, T.L.; Tsai, T.K.; Yang, H.P.; Huang, J.Z. Effect of ultra-fast laser texturing on surface wettability of microfluidic channels. *Microelectron. Eng.* **2012**, *98*, 684–688.
134. Demir, A.G.; Lecis, N.; Previtali, B.; Ugues, D. Scratch resistance of fibre laser surface textured tin coatings. *Surf. Eng.* **2013**, *29*, 654–659.
135. Tetsuo, S.; Nikolay, N.; Minoru, O. Friction characteristics of submicrometre-structured surfaces fabricated by particle-assisted near-field enhancement with femtosecond laser. *J. Phys. D Appl. Phys.* **2007**, *40*, 7485–7491.
136. Bathe, R.; Sai Krishna, V.; Nikumb, S.K.; Padmanabham, G. Laser surface texturing of gray cast iron for improving tribological behavior. *Appl. Phys. A* **2014**, *117*, 117–123.
137. Bereznai, M.; Pelsoczi, I.; Toth, Z.; Turzo, K.; Radnai, M.; Bor, Z.; Fazekas, A. Surface modifications induced by ns and sub-ps excimer laser pulses on titanium implant material. *Biomaterials* **2003**, *24*, 4197–4203.
138. Fadeeva, E.; Schlie, S.; Koch, J.; Chichkov, B.N.; Vorobyev, A.Y.; Guo, C.L. Femtosecond laser-induced surface structures on platinum and their effects on surface wettability and fibroblast cell proliferation. In *Contact Angle, Wettability and Adhesion*; Mittal, K.L., Ed.; CRC Press: Boca Raton, FL, USA, 2009; Volume 6, pp. 163–171.
139. Kenar, H.; Akman, E.; Kacar, E.; Demir, A.; Park, H.; Abdul-Khaliq, H.; Aktas, C.; Karaoz, E. Femtosecond laser treatment of 316L improves its surface nanoroughness and carbon content and promotes osseointegration: An *in vitro* evaluation. *Colloids Surf. B* **2013**, *108*, 305–312.
140. Jeong, Y.H.; Choe, H.C.; Brantley, W.A. Nanostructured thin film formation on femtosecond laser-textured Ti-35Nb-xZr alloy for biomedical applications. *Thin Solid Films* **2011**, *519*, 4668–4675.
141. Ranella, A.; Barberoglou, M.; Bakogianni, S.; Fotakis, C.; Stratakis, E. Tuning cell adhesion by controlling the roughness and wettability of 3D micro/nano silicon structures. *Acta Biomater.* **2010**, *6*, 2711–2720.
142. Papadopoulou, E.L.; Samara, A.; Barberoglou, M.; Manousaki, A.; Pagakis, S.N.; Anastasiadou, E.; Fotakis, C.; Stratakis, E. Silicon scaffolds promoting three-dimensional neuronal web of cytoplasmic processes. *Tissue Eng. Part C* **2010**, *16*, 497–502.
143. Vorobyev, A.Y.; Guo, C.L. Making human enamel and dentin surfaces superwetting for enhanced adhesion. *Appl. Phys. Lett.* **2011**, *99*, 193703.
144. Ahsan, M.S.; Ahmed, F.; Kim, Y.G.; Lee, M.S.; Jun, M.B.G. Colorizing stainless steel surface by femtosecond laser induced micro/nano-structures. *Appl. Surf. Sci.* **2011**, *257*, 7771–7777.
145. Vorobyev, A.Y.; Guo, C.L. Spectral and polarization responses of femtosecond laser-induced periodic surface structures on metals. *J. Appl. Phys.* **2008**, *103*, 043513.
146. Vorobyev, A.Y.; Makin, V.S.; Guo, C.L. Optical properties of femtosecond laser-induced periodic surface structures on metals. In Proceedings of the 52nd IEEE International Midwest Symposium on Circuits and Systems, Cancun, Mexico, 2–5 August 2009; pp. 909–912.
147. Dusser, B.; Sagan, Z.; Soder, H.; Faure, N.; Colombier, J.P.; Jourlin, M.; Audouard, E. Controlled nanostructures formation by ultra fast laser pulses for color marking. *Opt. Expr.* **2010**, *18*, 2913–2924.
148. Mahmood, A.; Venkatakrishnan, K.; Tan, B. 3-D aluminum nanostructure with microhole array synthesized by femtosecond laser radiation for enhanced light extinction. *Nanoscale Res. Lett.* **2013**, *8*, 1–8.

149. Wu, C.; Crouch, C.H.; Zhao, L.; Carey, J.E.; Younkin, R.; Levinson, J.A.; Mazur, E.; Farrell, R.M.; Gothoskar, P.; Karger, A. Near-unity below-band-gap absorption by microstructured silicon. *Appl. Phys. Lett.* **2001**, *78*, 1850–1852.
150. Vorobyev, A.Y.; Makin, V.S.; Guo, C.L. Brighter light sources from black metal: Significant increase in emission efficiency of incandescent light sources. *Phys. Rev. Lett.* **2009**, *102*, 234301.
151. Xu, B.; Wu, X.-Y.; Ling, S.-Q.; Luo, F.; Du, C.-L.; Sun, X.-Q. Fabrication of 3D metal micro-mold based on femtosecond laser cutting and micro-electric resistance slip welding. *Int. J. Adv. Manuf. Technol.* **2013**, *66*, 601–609.

© 2014 by the authors; licensee MDPI, Basel, Switzerland. This article is an open access article distributed under the terms and conditions of the Creative Commons Attribution license (<http://creativecommons.org/licenses/by/4.0/>).